

REPORT DOCUMENTATION PAGE

Form Approved
OMB No. 0704-0188

Public reporting burden for this collection of information is estimated to average 1 hour per response, including the time for reviewing instructions, searching existing data sources, gathering and maintaining the data needed, and completing and reviewing this collection of information. Send comments regarding this burden estimate or any other aspect of this collection of information, including suggestions for reducing this burden to Department of Defense, Washington Headquarters Services, Directorate for Information Operations and Reports (0704-0188), 1215 Jefferson Davis Highway, Suite 1204, Arlington, VA 22202-4302. Respondents should be aware that notwithstanding any other provision of law, no person shall be subject to any penalty for failing to comply with a collection of information if it does not display a currently valid OMB control number. PLEASE DO NOT RETURN YOUR FORM TO THE ABOVE ADDRESS.

1. REPORT DATE (DD-MM-YYYY) 12-12-2002		2. REPORT TYPE Final Technical Report		3. DATES COVERED (From - To) June 1999-June 2002	
4. TITLE AND SUBTITLE A New Approach for Prediction of Aircraft Spin				5a. CONTRACT NUMBER	
				5b. GRANT NUMBER F49620-00-1-0050	
				5c. PROGRAM ELEMENT NUMBER	
6. AUTHOR(S) Squires, Kyle D.				5d. PROJECT NUMBER	
				5e. TASK NUMBER	
				5f. WORK UNIT NUMBER	
7. PERFORMING ORGANIZATION NAME(S) AND ADDRESS(ES) Mechanical and Aerospace Engineering Department, Arizona State University, Tempe, AZ 85287-6106				8. PERFORMING ORGANIZATION REPORT NUMBER XAA 0090/TE	
9. SPONSORING / MONITORING AGENCY NAME(S) AND ADDRESS(ES) Air Force Office of Scientific Research / NA 4015 Wilson Blvd, Room 713 Arlington VA 22203-1954				10. SPONSOR/MONITOR'S ACRONYM(S) AFOSR	
				11. SPONSOR/MONITOR'S REPORT NUMBER(S)	
12. DISTRIBUTION / AVAILABILITY STATEMENT APPROVED FOR PUBLIC RELEASE.					
13. SUPPLEMENTARY NOTES					
14. ABSTRACT Unsteady Reynolds-averaged Navier-Stokes and Detached-Eddy Simulation are used to predict the flow around a forebody cross-section modeled by a rounded-corner square. The inlet velocity is inclined at 10 degrees to the main flow, the configuration modeling the massively separated flow around the forebody of a jet fighter rotating at high angle of attack. Simulations are performed at sub- and super-critical Reynolds numbers, corresponding to either laminar or turbulent boundary layer separation from the forebody. DES predictions show that following flow detachment, a chaotic and three-dimensional wake rapidly develops. The temporal evolution of the streamwise and lateral (side) forces acting on the body exhibit strong modulation due to the spanwise variation of the flow. Grid refinement deepens the structure of the resolved range of turbulent scales, predictions using unstructured meshes are also demonstrated to be equally accurate as those on structured grids. For the super-critical flow, the pressure distribution is close to the measured values, both the streamwise and side forces are in adequate agreement with measurements, and the effect of numerical parameters are well-understood. For the sub-critical flow, DES side-force predictions do not follow the experimental measurements far enough to achieve reversal. Possible causes for the discrepancy are discussed.					
15. SUBJECT TERMS turbulence simulation, turbulent modeling, unsteady flow, high Reynolds numbers, massive separations					
16. SECURITY CLASSIFICATION OF:			17. LIMITATION OF ABSTRACT	18. NUMBER OF PAGES 48	19a. NAME OF RESPONSIBLE PERSON Kyle D. Squires
a. REPORT	b. ABSTRACT	c. THIS PAGE			19b. TELEPHONE NUMBER (include area code) (480) 965-3957

20021231 078

A New Approach to Prediction of Aircraft Spin

Kyle D. Squires
Mechanical and Aerospace Engineering Department
Arizona State University
P.O. Box 876106
Tempe, AZ 85287 USA

Sponsored by:
Air Force Office of Scientific Research



Executive Summary

The accurate simulation and modeling of massively separated flows comprises one of the primary obstacles in application of Computational Fluid Dynamics (CFD) as a more routinely used tool in engineering design and analysis. The work reported here represents the first step in a program in which the long-term objective is the development of a CFD tool for predicting aircraft spin. Such a tool will offer numerous advantages over current approaches to predicting spin characteristics, as well as other related phenomena. The particular focus is on modeling massive separations using Detached-Eddy Simulation (DES), a hybrid method that combines Reynolds-averaged Navier-Stokes (RANS) approaches with Large Eddy Simulation (LES). The primary vehicle for assessing the simulation methodology was prediction of the flow around a model of an aircraft forebody, in crossflow with the freestream at angle of attack. The flow at angle of attack is sensitive to the Reynolds number with experimental measurements showing that the side force reverses sign with increases in Reynolds number, a reversal being crucial as it propels the spin of an actual forebody.

Side-force reversal is dependent on the state of the separating boundary layer, i.e., laminar or turbulent, and in the first phase of the work, treatment of boundary layer separation is assessed using calculations of the two-dimensional separated flows around two configurations: a rounded-corner square with the corner radius of the model equal to 1/4 of the body width/diameter, and a 2:1 ellipse. The incompressible flow around the configurations is predicted using a fractional step method developed for application in curvilinear coordinates. A grid generation scheme was developed using the control technique of Hsu and Lee (1991) for creation of structured meshes and used for gridding both geometries. This method assures orthogonality of the grid at boundaries and control over the spacing to the first mesh point within the domain. The simulation approach for this phase of the work was based on solution of the unsteady RANS (URANS) equations with the Reynolds stress closed using the Spalart-Allmaras one-equation model. Characteristics of the separating boundary layer are established by the inlet conditions. For flows with turbulent boundary layer separation, a small level of eddy viscosity is prescribed at the inlet to the computational domain, sufficient to activate the turbulence model as the fluid contacts the forebody. Separation of laminar boundary layers is accomplished using the "tripless" approach of Travin *et al.* (2001) in which the initial eddy viscosity within the domain is non-zero and the inlet eddy viscosity is zero. The separating boundary layer is laminar, recirculation in the wake of the body is sufficient to sustain the model. Simulation results for each configuration show that both approaches are viable, with the distinctly different boundary layer separation characteristics achieved, leading to changes in the pressure coefficient and skin friction distributions around the body.

In the second phase of the work, URANS and DES are used to predict the flow around the forebody cross-section modeled by the rounded-corner square, the same cross-section considered in the first phase of the study. The inlet velocity is inclined at 10° to the main flow, the configu-

ration modeling the massively separated flow around the forebody of a jet fighter rotating at high angle of attack. The geometry is uniform (extruded) along the statistically homogeneous spanwise coordinate for which periodic boundary conditions were applied. Simulations are performed at a sub-critical Reynolds number of 10^5 (based on the freestream speed and body width/diameter) for which the separating boundary layer is laminar and a super-critical Reynolds number of 8×10^5 for which the separating boundary layer is turbulent. Between these Reynolds numbers experimental measurements show a reversal of the side force. DES predictions are evaluated using experimental measurements and contrasted with the URANS predictions. The role of the grid is assessed, initially through grid refinement performed using structured grids. Subsequently, the use of unstructured grids for simulations of unsteady, eddy-resolving turbulent flows is also assessed. The unstructured grids are comprised of nearly isotropic tetrahedra away from solid surfaces while the boundary layers are comprised of prisms. DES predictions show that following flow detachment, a chaotic and three-dimensional wake rapidly develops. The temporal evolution of the streamwise and lateral (side) forces acting on the body exhibit strong modulation due to the spanwise variation of the flow. Grid refinement deepens the structure of the resolved range of turbulent scales, the predictions on unstructured meshes are also demonstrated to be equally accurate as those on structured grids. For the super-critical flow, the pressure distribution is close to the measured values, both the streamwise and side forces are in adequate agreement with measurements, and the effect of numerical parameters are well-understood. For the sub-critical flow, DES side-force predictions do not follow the experimental measurements far enough to achieve reversal. Possible causes for the discrepancy are discussed.

Contents

Executive Summary	i
Contents	iii
1 Introduction and Overview	1
1.1 Background: Spin	1
1.2 Background: Hybrid methods for predicting high Reynolds number flows	3
2 Objectives and summary of the approach	5
3 Approach	6
3.1 Detached-Eddy Simulation	6
3.2 Numerical methods	9
3.2.1 Incompressible flow solver	9
3.2.2 Compressible flow solver	14
3.3 Flow configuration and simulation design	15
4 Results	17
4.1 Two-dimensional computations – URANS	17
4.2 Three-dimensional computations – DES and URANS	21
5 Summary and Perspectives	27

1 Introduction and Overview

Knowledge of the spin and recovery characteristics of modern aircraft is crucial at a variety of levels, including maneuverability, control strategies, and ultimately design. One of the most significant factors affecting spin characteristics for modern fighters is the forebody, with its complex vortical flows and long moment arm. Laboratory measurements of spin characteristics are of limited utility since it is not possible to resolve important Reynolds number effects because of the range of available tunnels. Numerical simulation, therefore, provides an important tool that should ultimately provide higher-fidelity evaluations of aircraft spin than current approaches.

Predicting the physics of spin has remained a substantial challenge to modeling approaches, e.g., the flows are characterized by unsteady massive separation and the dependence on transition. Simulation techniques used for prediction of these phenomena at high Reynolds numbers have traditionally relied on Reynolds-averaged approaches which are unable to represent these physics to sufficient accuracy. The enormous computational requirements to resolve boundary layers using techniques which incorporate more flow details, such as Large Eddy Simulation (LES), will prevent their application to whole domains at the Reynolds number ranges encountered in applications for the foreseeable future (e.g., see Spalart *et al.* 1997, Spalart 2000).

Unfortunately, the performance of numerical models has been inaccurate in most instances due to their inability to accurately predict the complex and unsteady effects associated with spin. Vortical flows, crossflow separations, and sensitivity of forces and moments to Reynolds number greatly challenge modeling approaches. These factors also supply the overall motivation for the present fundamental investigations and the need to develop and assess improved techniques for predicting complex, separated flows at high Reynolds numbers.

1.1 Background: Spin

The characteristic motion of an aircraft following stall in which the plane descends rapidly along a more or less helical trajectory is known as the spin. Spin has been an important problem for civil and military aircraft since the beginning of flight (see Durand 1934 and Anderson 1979 for historical reviews). While important, prediction of spin characteristics is difficult and is dependent upon a large number of aerodynamic parameters, including slope of the lift curve top, rolling moment, roll and yaw damping, pitching and yawing moments, etc. While stable at low angle of attack, some of these rotary derivatives can change sign at stall, remain unstable at high attack angles and promote spin.

Early spin models were developed from force and moment equilibrium under steady conditions (e.g., see Tischler & Barlow 1980 and references therein). The objective was to identify those factors most affecting the balance of forces and moments during a steady spin and to use linear analyses to consider dynamic behavior for states near the steady spin. Linear theories, while able

to predict some aspects of steady spins, cannot account for important, and highly nonlinear, effects such as sideslip.

Most of what is known about spin modes has been derived from rotary balance data (e.g., see Bihrlé *et al.* 1978, Hultberg *et al.* 1980). Recent measurements and analysis of rotary balance data obtained at the Air Force Research Laboratory (AFRL), while not directly considering spin, provides an illustration of the complex fluid mechanics which challenge predictions (Jenkins *et al.* 1996, Jobe *et al.* 1996, Grismer & Jenkins 1997, Jenkins 1997). Reported in these investigations are in-depth studies of a 65 degree delta wing at high angles of attack. The main focus was on the complex development of the leading-edge vortices in regimes where vortex breakdown occurs. Aerodynamic reactions are sensitive to breakdown and related phenomena which occur over disparate time scales. Because linear models cannot account for these effects, subsequent efforts have focused on development of nonlinear models with time constants in aerodynamic response determined from measurements (e.g., see Tobak & Chapman 1985, Troung & Tobak 1990, Myatt 1997).

Simulation work relevant to the the research reported here includes the solutions of the unsteady, three-dimensional compressible Navier-Stokes equations of the flow around the delta wing, but at lower Reynolds number, than considered in the AFRL rotary measurements. The objective was to determine if yaw rate effects evident in coning motions from rotary balance tests will significantly change the mean location of vortex breakdown. Tromp (1998) investigated effects of roll and yaw rates by considering the responses from a coning motion and a pure roll-rate helical motion. Tromp found that the movement in vortex breakdown location with yaw rate was relatively small, suggesting that using coning motion to estimate the rate effects on critical states may provide reasonable estimations.

An effect recognized to be important, but not considered in the work summarized above is that of the Reynolds number. Though spin characteristics are known to exhibit strong sensitivity to Reynolds number (e.g., see McCormick 1981), there have been relatively few investigations of Reynolds number effects in spin or spin-related flows. One attempt is the work reported by Fritz (1995), who used RANS computations to predict spin characteristics of generic forebody cross-sections. Two-dimensional solutions were compared to two-dimensional wind tunnel data of Polhamus *et al.* (1959) and a strip theory method was used to integrate the solutions to compare with data gathered for four generic, rotary balance models. Fritz (1995), while able to predict the proper spin in super-critical Reynolds number regimes, was unable to predict the proper spin in sub-critical regimes. The major difficulties encountered were correctly and consistently predicting the location of flow separation and the inability of turbulence models to handle the varying length scales of separated, bluff body flows.

The lack of reliable methods for handling Reynolds number variations severely limits CFD for predicting spin and improved approaches have long been sought. Experimental resolution of

Reynolds number effects requires costly and time-consuming tests, probably using more than one wind tunnel. Models of aerodynamic response require some calibration using either experiments or simulations. Unfortunately, previous computational efforts have not considered Reynolds number effects or have been unable to predict spin characteristics over a range of Reynolds numbers using available strategies, i.e., RANS techniques without clear control of transition. The drawback of current simulation strategies based on solution of the Reynolds-averaged Navier-Stokes equations is that accurate prediction of spin requires accurate prediction of geometry-dependent, unsteady three-dimensional turbulent motions which are very important in the separated flows characterizing spin. These eddies, arguably, are what defeats traditional RANS turbulence models, of any complexity. Presented next is an overview of methods used for predicting complex flows at high Reynolds numbers, an overview that is used to provide the context for the technique forming the backbone for this research: Detached-Eddy Simulation.

1.2 Background: Hybrid methods for predicting high Reynolds number flows

Most high-Reynolds number predictions are currently obtained from solutions of the Reynolds-averaged Navier-Stokes (RANS) equations. While the most popular RANS models appear to yield predictions of useful accuracy in attached flows as well as some with shallow separations, RANS predictions of massive separations have typically been unreliable. RANS models, calibrated in thin shear layers, appear unable to consistently represent to sufficient accuracy the geometry-dependent, chaotic and unsteady features of massively separated flows. This is the case even with unsteady RANS, which is often capable of producing vortex shedding, though shedding from URANS predictions is typically non-chaotic and exaggerated in amplitude (e.g., see Travin *et al.* 2001). URANS predictions of drag, for example, have typically been too high, though it should be recognized that this pessimistic view of URANS is not a universal one (Durbin 1995).

The relatively poor performance of RANS models has motivated the increased application of Large Eddy Simulation (LES). Away from solid surfaces, LES is a powerful approach, providing a description of the large, energy-containing scales of motion that are typically dependent on geometry and boundary conditions. When applied to boundary layers, however, the computational cost of whole-domain LES does not differ significantly from that of Direct Numerical Simulation (DNS) (Spalart *et al.* 2000). The “large eddies” close to the wall are physically small in scale, in a whole-domain LES (i.e., without wall modeling), these small near-wall structures are dynamically important and must be resolved in order to accurately predict boundary layer evolution. In boundary layers without sufficient resolution of the wall-layer structures, LES predictions of boundary layer growth and/or separation will be adversely affected.

These and other considerations provided the motivation for development of Detached-Eddy Simulation (DES) by Spalart *et al.* (1997). DES belongs to the class of hybrid methods which

attempt to combine RANS and LES, exploiting the accuracy and efficiency of RANS approaches in the thin shear layers not far from the calibration range of the model, and LES for direct resolution of the geometry-dependent and three-dimensional eddies in regions where such a treatment is desired. DES was developed independently of a different approach proposed by Speziale (1998) also aimed at combining RANS and LES. Speziale (1998) proposed damping the Reynolds stress predicted by a second-moment closure approach, $\langle u_i u_j \rangle^{(M)}$, by a factor α ,

$$\langle u_i u_j \rangle = \alpha \langle u_i u_j \rangle^{(M)}, \quad (1)$$

where $\alpha < 1$. The Reynolds stress $\langle u_i u_j \rangle$ on the left-hand side (1) is then supplied to the momentum equations. Speziale (1998) proposed that the damping α be determined based on a measure of the local resolution compared to the Kolmogorov scale,

$$\alpha = \left[1 - \exp(-\beta(L_\Delta/L_K)) \right]^n, \quad (2)$$

where L_Δ is a lengthscale related to the grid size, L_K is the Kolmogorov lengthscale and β and n are adjustable parameters. Two limits of (2) are well defined. The first limit corresponds to the “RANS limit” of the model for which $L_\Delta \gg L_K$ in which case $\alpha \rightarrow 1$ and the Reynolds stress supplied to the momentum equations is identical to that obtained from the particular second-moment closure being employed. The second limit corresponds to the “DNS limit” for which $L_\Delta \ll L_K$ in which $\alpha \rightarrow 0$ and the Reynolds stress supplied to the governing equations vanishes. Intermediate between these regimes the damping factor α will be less than unity, corresponding to only a fraction of the model stress $\alpha \langle u_i u_j \rangle^{(M)}$ predicted using the second-moment closure being supplied to the Navier-Stokes equations. In this intermediate range, therefore, part of the turbulent stress is modeled, the remaining part to be resolved directly on the mesh. This intermediate regime corresponding to the “LES regime” of the model. An important question is the response of the model in its “LES regime” for computations in which $L_\Delta \gg L_K$, the criteria also used to define the “RANS region”, i.e., the form of the model should be fundamentally different in the RANS and LES limits though it appears from (1) and (2) that there could be some ambiguity when $L_\Delta \gg L_K$. Von Terzi and Fasel (2002) have adopted the basic outline of the above approach, one of the main modifications being the introduction of a “contribution function” which plays a similar role as α in (2), dictating the level of the turbulent stress to be modeled versus resolved.

Batten *et al.* (2000) have developed a hybrid RANS-LES method referred to as Limited Numerical Scales (LNS). The approach appears to be very similar to DES, the method reducing to a RANS treatment of the boundary layer and LES away from solid surfaces. The relation (1) comprised the basis for the initial form of the model, though rather than defining α using (2), Batten *et al.* (2000) propose to base α essentially on a ratio of eddy viscosities in the RANS and LES regions,

$$\alpha = \frac{\min((Lv)_{LES}, (Lv)_{EA})}{(Lv)_{EA}}, \quad (3)$$

where $(Lv)_{LES}$ represents a lengthscale-velocity product obtained from an LES model and $(Lv)_{EA}$ represents a lengthscale-velocity product obtained from an ensemble-averaged model.

As described in greater detail in §3.1, DES has RANS behavior near the wall and becomes a Large Eddy Simulation in the regions away from solid surfaces provided the grid density is sufficient. The formulation is based on a modification to the Spalart-Allmaras one-equation model (Spalart and Allmaras 1994, referred to as S-A throughout). Some of the principle advantages of DES are that the technique is non-zonal and computationally feasible for high Reynolds number prediction, but also resolves time-dependent, three-dimensional turbulent motions as in LES.

A recent review of some of the applications of DES can found in Strelets (2001). DES has predicted to much higher accuracy than traditional approaches the flow around an airfoil at high angle of attack, another necessary pre-requisite for prediction of spin (Shur *et al.* 1999). DES has also been used to successfully predict the flow around a sphere, an important benchmark, resolving the time-dependent forces around the body to a higher accuracy than methods based on the Reynolds-averaged Navier-Stokes (RANS) equations, and in a Reynolds number range higher than can be realistically attempted using full-domain LES (Constantinescu *et al.* 2002). An important outcome of these studies is that the cost of DES exhibits a weak dependence on Reynolds number, no worse than RANS methods.

Because the boundary layer is predicted by the S-A model, the empirical input to the technique, as true for all hybrid methods, is not small and in DES, for example, the prediction of boundary layer separation is under control of the RANS model. Assessing the technique, therefore, remains an important task, not only with respect to aspects such as predicting boundary layer separation (the primary consideration of the first part of this work), but also the response of the method to the numerical approach, e.g., the grid and timestep, which are some of the other aspects scrutinized in the second part of the work.

2 Objectives and summary of the approach

The research described in this report is a pre-cursor to the ultimate application which is prediction of the spin characteristics of full aircraft at flight Reynolds numbers. The flow fields characterizing spinning aircraft are massively separated, providing a “natural” application for DES and therefore the principle objective was to apply and assess the method in a flow important to understanding and accurately predicting spin. Though a natural application for the model, calculations of complex configurations at high Reynolds numbers challenge the entire computational approach, including numerical aspects related to features such as grid generation and grid type (i.e., structured or unstructured), to aspects impacting the physical modeling, an issue of primary importance being the treatment of the separating boundary layer.

The work is divided into two parts. For spin prediction, a key issue is the sign of the side force,

and whether the side force is spin-damping or spin-propelling. The side force, both in magnitude and sign, is dependent the state of the separating boundary layer, i.e., whether the separating boundary layer is laminar or turbulent. In the context of hybrid methods, for which boundary layer separation is under control of the RANS model, the type of transition is controlled by the eddy viscosity using the S-A model. In the first phase of the work, calculations of two-dimensional flows were used to investigate approaches for controlling the type of boundary layer separation and to assess viability for the more computationally-intensive three-dimensional calculations performed in the second phase of the work.

In the second phase of the work the factors included in the investigation include the role of the grid, assessment of the flow solver and treatment of boundary layer detachment for three-dimensional configurations. Given the end application of full-aircraft configurations, unstructured grids form an integral component of the present approach and therefore an unstructured-grid solver was employed for numerical solution of the Navier-Stokes equations for the three-dimensional calculations.

The disadvantage of the current unstructured approach is that the numerical procedure is only second-order accurate in time and space and stabilized via non-linear (TVD) numerical dissipation. Related investigations have shown that the artificial dissipation associated with the numerical scheme can be as large as that represented by the turbulence model and therefore care must be exercised in application of these methods to eddy-resolving simulations such as LES (e.g., see Mittal and Moin 1997). This in turn motivates another goal of the present effort – to explore the accuracy of the current second-order method on both structured and unstructured grids for DES applications. This is not a simple matter of verifying the order of accuracy, which is difficult to define and predict in LES and especially hybrid methods. Nevertheless, the primary tool for such a study remains grid refinement.

3 Approach

3.1 Detached-Eddy Simulation

Detached Eddy Simulation (DES) is a hybrid technique first proposed by Spalart *et al.* (1997) for prediction of turbulent flows at high Reynolds numbers (see also Spalart 2000). The motivation for developing DES was to combine the most favorable aspects of RANS and LES, i.e., the acceptable predictions using RANS models of thin shear layers and LES for resolution of time-dependent, three-dimensional large eddies which are typically geometry-dependent. RANS models are less accurate in separated regions than in the thin shear layers where they are calibrated. In these regions LES is very attractive since the large scales can be resolved without the vast increases in grid resolution necessary in LES of boundary layers.

The DES formulation is based on a modification to the S-A model such that it reduces to

RANS close to solid surfaces and to LES away from the wall (Spalart *et al.* 1997). The S-A RANS model of Spalart and Allmaras (1994) is summarized below along with a discussion of the DES formulation. Additional discussion can be found in Spalart (2000) and Strelets (2001).

In the S-A RANS model, a transport equation is used to compute a working variable used to form the turbulent eddy viscosity,

$$\begin{aligned} \frac{D\tilde{\nu}}{Dt} = & c_{b1}\tilde{S}\tilde{\nu} - \left[c_{w1}f_w - \frac{c_{b1}}{\kappa^2}f_{t2} \right] \left[\frac{\tilde{\nu}}{d} \right]^2 \\ & + \frac{1}{\sigma} \left[\nabla \cdot ((\nu + \tilde{\nu})\nabla\tilde{\nu}) + c_{b2}(\nabla\tilde{\nu})^2 \right] + f_{t1} \Delta U^2, \end{aligned} \quad (4)$$

where $\tilde{\nu}$ is the working variable. The eddy viscosity ν_t is obtained from,

$$\nu_t = \tilde{\nu} f_{v1}, \quad f_{v1} = \frac{\chi^3}{\chi^3 + c_{v1}^3}, \quad \chi \equiv \frac{\tilde{\nu}}{\nu}, \quad (5)$$

where ν is the molecular viscosity. The production term is expressed as,

$$\tilde{S} \equiv f_{v3}S + \frac{\tilde{\nu}}{\kappa^2 d^2} f_{v2}, \quad (6)$$

$$f_{v2} = \left(1 + \frac{\chi}{c_{v2}} \right)^{-3}, \quad f_{v3} = \frac{(1 + \chi f_{v1})(1 - f_{v2})}{\chi}, \quad (7)$$

where S is the magnitude of the vorticity. The production term as written in (6) differs from that developed in Spalart and Allmaras (1994) via the introduction of f_{v3} and re-definition of f_{v2} . These changes do not alter predictions of fully turbulent flows and have the advantage that for simulation of flows with laminar separation, spurious upstream propagation of the eddy viscosity into attached, laminar regions is prevented. The function f_w is given by,

$$f_w = g \left[\frac{1 + c_{w3}^6}{g^6 + c_{w3}^6} \right]^{1/6}, \quad g = r + c_{w2}(r^6 - r), \quad r \equiv \frac{\tilde{\nu}}{\tilde{S}\kappa^2 d^2}. \quad (8)$$

The function f_{t2} is defined as,

$$f_{t2} = c_{t3} \exp(-c_{t4}\chi^2). \quad (9)$$

The trip function f_{t1} is specified in terms of the distance d_t from the field point to the trip, the wall vorticity ω_t at the trip, and ΔU which is the difference between the velocity at the field point and that at the trip,

$$f_{t1} = c_{t1}g_t \exp \left(-c_{t2} \frac{\omega_t^2}{\Delta U^2} [d^2 + g_t^2 d_t^2] \right), \quad (10)$$

where $g_t = \min(0.1, \Delta U/\omega_t \Delta x)$ and Δx is the grid spacing along the wall at the trip. The wall boundary condition is $\tilde{\nu} = 0$. As described in §4, the inlet condition on $\tilde{\nu}$ was prescribed for either fully turbulent boundary layers prior to separation or with zero upstream values of $\tilde{\nu}$ that yielded laminar boundary layers prior to separation. The constants are $c_{b1} = 0.1355$, $\sigma = 2/3$, $c_{b2} = 0.622$,

$\kappa = 0.41$, $c_{w1} = c_{b1}/\kappa^2 + (1 + c_{b2})/\sigma$, $c_{w2} = 0.3$, $c_{w3} = 2$, $c_{v1} = 7.1$, $c_{v2} = 5$, $c_{t1} = 1$, $c_{t2} = 2$, $c_{t3} = 1.1$, and $c_{t4} = 2$.

The DES formulation is obtained by replacing the distance to the nearest wall, d , by \tilde{d} , where \tilde{d} is defined as,

$$\tilde{d} \equiv \min(d, C_{DES}\Delta), \quad (11)$$

with

$$\Delta \equiv \max(\Delta x, \Delta y, \Delta z). \quad (12)$$

where Δx , Δy , and Δz are the grid spacings. In “natural” applications of DES, the wall-parallel grid spacings (e.g., streamwise and spanwise) are at least on the order of the boundary layer thickness and the S-A RANS model is retained throughout the boundary layer, i.e., $\tilde{d} = d$. Consequently, prediction of boundary layer separation is determined in the ‘RANS mode’ of DES. Away from solid boundaries, the closure is a one-equation model for the SGS eddy viscosity. When the production and destruction terms of the model are balanced, the length scale $\tilde{d} = C_{DES}\Delta$ in the LES region yields a Smagorinsky eddy viscosity $\tilde{\nu} \propto S\Delta^2$. Analogous to classical LES, the role of Δ is to allow the energy cascade down to the grid size; roughly, it makes the pseudo-Kolmogorov length scale, based on the eddy viscosity, proportional to the grid spacing. “Wall distance” is the distance to the nearest wall, which can be clearly defined even in complex, fully three-dimensional geometries with multiple length scales. The additional model constant $C_{DES} = 0.65$ was set in homogeneous turbulence (Shur *et al.* 1999) and is used without modification in this work.

There are several advantages to the DES formulation described above. The transition between RANS and LES is seamless in a formulation sense: single equation, no explicit declaration of RANS versus LES zones. The solutions shown below show that the DES is seamless in an application sense, i.e., no artificial transitions between the solution domains. There is one solution field, all coupled by the Navier-Stokes equations, and the solution has a different character in different regions.

A further advantage of the length scale switch in DES is that it allows the user to ‘steer’ the physics where needed, i.e., finer resolution in regions where the additional flow detail from an LES treatment is desired. The length scale switch in the model has the effect of drawing down the eddy viscosity so the modeled equation can allow development of instabilities, which then feed a cascade to smaller scales, limited by the grid as in canonical LES. Regions of the flow not far from the thin shear layer approximation are very expensive to resolve using LES, and can be adequately handled by the S-A model within a RANS treatment. Important for applications is that the increase in cost of DES with Reynolds number is weak, similar to RANS, unlike in full-domain LES in which there is an enormous increase in cost because of the rapid increase in resolution requirements near walls (see also Nikitin *et al.* 2000).

3.2 Numerical methods

3.2.1 Incompressible flow solver

The approach to investigation of boundary layer separation characteristics for the first phase of the study was based on solution of the incompressible Reynolds-averaged Navier-Stokes equations. A code for implementation of a fractional-step numerical method was developed, the basic aspects of the numerical approach are outlined in this section.

The unsteady incompressible Navier-Stokes equation written in tensor form are expressed as,

$$\frac{\partial u_i}{\partial x_i} = 0, \quad (13)$$

$$\frac{\partial u_i}{\partial t} + \frac{\partial u_i u_j}{\partial x_j} = -\frac{1}{\rho} \frac{\partial p}{\partial x_i} + \frac{\partial}{\partial x_j} \nu \left[\frac{\partial u_i}{\partial x_j} + \frac{\partial u_j}{\partial x_i} \right], \quad (14)$$

where the velocity is denoted u_i , the pressure p , density ρ , and ν is the fluid kinematic viscosity. Non-dimensionalizing the above using a characteristic length L and characteristic velocity u_∞ results in a re-definition of the lengths, time, and dependent variables,

$$u_i = u_i/u_\infty, \quad x_i = x_i/L, \quad p = \frac{p}{\rho u_\infty^2}, \quad t = t u_\infty/L, \quad (15)$$

and the corresponding form of the non-dimensionalized equations,

$$\frac{\partial u_i}{\partial t} + \frac{\partial}{\partial x_j} (u_i u_j) = -\frac{\partial p}{\partial x_i} + \frac{\partial}{\partial x_j} \frac{\nu}{u_\infty L} \left[\frac{\partial u_i}{\partial x_j} + \frac{\partial u_j}{\partial x_i} \right] \quad (16)$$

The numerical approach to approximation of the above system is based on integration of (16) over an arbitrary (fixed) control volume V ,

$$\begin{aligned} \int_V \frac{\partial u_i}{\partial t} dV &= \int_V \frac{\partial}{\partial x_j} (-u_i u_j) dV + \int_V \frac{\partial}{\partial x_j} (-p) dV \\ &+ \int_V \frac{\partial}{\partial x_j} \frac{1}{Re} \left[\frac{\partial u_i}{\partial x_j} + \frac{\partial u_j}{\partial x_i} \right] dV, \end{aligned} \quad (17)$$

with the Reynolds number $Re = u_\infty L/\nu$. The equations can be cast equivalently in vector form as,

$$\begin{aligned} \int_V \frac{\partial \bar{\mathbf{u}}}{\partial t} dV &= \int_V \nabla \cdot (-\bar{\mathbf{u}} \bar{\mathbf{u}}) dV + \int_V \nabla \cdot (-P \bar{\mathbf{I}}) dV \\ &+ \int_V \nabla \cdot \frac{1}{Re} \left[\nabla \bar{\mathbf{u}} + (\nabla \bar{\mathbf{u}})^T \right] dV, \end{aligned} \quad (18)$$

where $\bar{\mathbf{u}} \bar{\mathbf{u}}$ is a dyad (second order tensor). Using Gauss' theorem, $\int_V \nabla \cdot \mathbf{A} dV = \int_S \mathbf{A} \cdot d\mathbf{S}$, the equations governing the constant-density and isothermal flow over the fixed control volume V with surface S can finally be written as,

$$\int_S \bar{\mathbf{u}} \cdot d\mathbf{S} = 0 \quad (19)$$

$$\int_V \frac{\partial \bar{\mathbf{u}}}{\partial t} dV = \int_S \bar{\mathbf{T}} \cdot d\mathbf{S}, \quad (20)$$

where $\bar{\mathbf{T}}$ is given in operator form as,

$$\bar{\mathbf{T}} = -\bar{\mathbf{u}}\bar{\mathbf{u}} - P\bar{\mathbf{I}} + \frac{1}{Re} [\nabla \bar{\mathbf{u}} + (\nabla \bar{\mathbf{u}})^T], \quad (21)$$

or in tensor notation expressed as

$$\bar{T}_{ij} = -u_i u_j - P\delta_{ij} + \frac{1}{Re} \left[\frac{\partial u_i}{\partial x_j} + \frac{\partial u_j}{\partial x_i} \right]. \quad (22)$$

Coordinate transformation

The equations (19) and (20) are solved in a general curvilinear system that is simplified for the present investigations to two-dimensional configurations, i.e., with a uniform (non-transformed) spanwise coordinate z . The first step in solution of (19) and (20) is consideration of the coordinate transformation of a vector \mathbf{R} from the Cartesian system to a curvilinear non-orthogonal system as shown schematically in Figure 1a, $\mathbf{R}(x, y, z) \rightarrow \mathbf{R}(\xi, \eta, z)$.

In what follows, the natural local base of the transformed curvilinear coordinate system (ξ, η, z) is denoted $\mathbf{e}_q = \partial \mathbf{r} / \partial q$, $q = \xi, \eta, z$. The transformation between the two systems is achieved by defining a new base in terms of the vector product of the natural local basis \mathbf{e}_q , $\mathbf{S}^q = \mathbf{e}_{q+1} \times \mathbf{e}_{q+2}$ (q , cyclic permutation). Note that the vector \mathbf{S}^q has a magnitude equal to the area of the parallelogram spanned by natural local basis $(\mathbf{e}_{q+1}, \mathbf{e}_{q+2})$ and is perpendicular to the plane defined by $(\mathbf{e}_{q+1}, \mathbf{e}_{q+2})$. Using the orthogonality between the new basis \mathbf{S}^q and its reciprocal base \mathbf{S}_q , the series operations in generalized curvilinear systems as outlined below will naturally yield dependent variables that are the volume fluxes, rather than the primitive variables.

At an arbitrary point (i, j, k) within the domain, the area tensor is defined as,

$$\mathbf{S} = (\mathbf{S}^\xi, \mathbf{S}^\eta, \mathbf{S}^z), \quad (23)$$

where the vector components are defined as,

$$\mathbf{S}^\xi = \frac{\partial \mathbf{r}}{\partial \eta} \times \frac{\partial \mathbf{r}}{\partial z}, \quad \mathbf{S}^\eta = \frac{\partial \mathbf{r}}{\partial z} \times \frac{\partial \mathbf{r}}{\partial \xi}, \quad \mathbf{S}^z = \frac{\partial \mathbf{r}}{\partial \xi} \times \frac{\partial \mathbf{r}}{\partial \eta}, \quad (24)$$

or in a more compact form,

$$\mathbf{S}^q = \frac{\partial \mathbf{r}}{\partial(q+1)} \times \frac{\partial \mathbf{r}}{\partial(q+2)} \quad (25)$$

where $q = \xi, \eta, z$ are in cyclic order. The vector quantity \mathbf{S}^q has the magnitude of the area of the face and direction given by the normal of the face (c.f., Figure 1b).

The partial derivative of the position vector $\mathbf{r}(x(\xi, \eta), y(\xi, \eta), z)$ with respect to ξ, η, z are evaluated using a central finite difference approximation. For example, with reference to Figure 1b,

$$\left. \frac{\partial \mathbf{r}}{\partial \xi} \right|_P = \frac{\mathbf{r}[x(\xi, \eta, z), y(\xi, \eta), z]_e - [x(\xi, \eta, z), y(\xi, \eta), z]_w}{\Delta \xi}. \quad (26)$$

The area vectors S^q are required to satisfy geometric constraints, the first of which is that for any computational cell within the domain the cell should be closed, i.e.,

$$\int \int_S dS = 0, \quad (27)$$

or in discrete form,

$$\sum_q S^q = 0. \quad (28)$$

To satisfy (26) to machine accuracy in the computation, $\partial r / \partial q$ needs to be consistently evaluated with respect to the computational grid points. In the present computations, the area vectors S_q and their reciprocal bases evaluated and stored at cell centers. Area vectors at cell faces are obtained via simple arithmetic averaging.

The volume of the computational cell is evaluated from

$$V = \frac{S_w^\xi + S_s^\eta + S_b^z}{3} \cdot (r_{fne} - r_{bsw}), \quad (29)$$

with the geometric constraint on the volumes specified as,

$$\sum_{cells} V = V_{domain}. \quad (30)$$

Discretization of the continuity and momentum equations

The continuity constraint is discretized in its integral form, applied to a given computational volume and with reference to Figure 1b takes the form,

$$(S^\xi \cdot \bar{u})_e - (S^\xi \cdot \bar{u})_w + (S^\eta \cdot \bar{u})_n - (S^\eta \cdot \bar{u})_s + (S^z \cdot \bar{u})_f - (S^z \cdot \bar{u})_b = 0. \quad (31)$$

The form (31) suggests dependent variables different than the primitive variables. The quantities in (31) represent volume fluxes and can be formally defined,

$$u^\xi = S^\xi \cdot \bar{u} = S_x^\xi u_i + S_y^\xi u_j + S_z^\xi u_k \quad (32)$$

$$u^\eta = S^\eta \cdot \bar{u} = S_x^\eta u_i + S_y^\eta u_j + S_z^\eta u_k \quad (33)$$

$$u^z = S^z \cdot \bar{u} = S_x^z u_i + S_y^z u_j + S_z^z u_k \quad (34)$$

where u^ξ, u^η, u^z are the volume fluxes over the ξ, η, z faces of a primary control volume, and u_i, u_j, u_k are the Cartesian velocity components.

The introduction of the volume fluxes leads to the continuity constraint expressed as,

$$u_e^\xi - u_w^\xi + u_n^\eta - u_s^\eta + u_f^z - u_b^z = 0 \quad (35)$$

where $u^q = (u^\xi, u^\eta, u^z)$. An advantage of the use of volume fluxes and continuity constraint written as (35) is that global mass conservation is easily expressed via,

$$\sum_{\text{total cell faces}} u^q = 0 \quad (36)$$

The integral form of the momentum equation with Cartesian velocity components as unknown variables is rewritten below,

$$\int \int \int_V \frac{\partial \bar{u}}{\partial t} dV = \int \int_S \bar{T} \cdot dS. \quad (37)$$

Approximating the above over an arbitrary (and fixed) control volume V yields,

$$V \frac{\partial \bar{u}}{\partial t} = \sum_q S^q \cdot \bar{T} = F \quad (38)$$

where F represents the total flux through the computational cell.

Using the relations (32)-(34), the momentum equations along direction q with u^ξ, u^η, u^z as variables are,

$$S^q \cdot (V \frac{\partial \bar{u}}{\partial t}) = V \frac{\partial u^q}{\partial t} = S^q \cdot F \quad (39)$$

where $q = \xi$ or η or z . The momentum equations in the form (39) are those considered next for numerical approximation.

Fractional step method

Writing (39) for the ξ direction, with reference to Figure 1b,

$$V_\xi \frac{\partial u^\xi}{\partial t} = S^\xi \cdot F = S^\xi \cdot [\sum_q S^q \cdot \bar{T}] = L_\xi, \quad (40)$$

The linear operator L_ξ is split into several parts,

$$L_\xi = H_\xi + R_\xi + D_\xi + D_{\xi,ex}, \quad (41)$$

where H_ξ are the nonlinear convection terms, R_ξ the pressure term, D_ξ are the diffusion terms that are advanced implicitly, and $D_{\xi,ex}$ represents the diffusion terms advanced explicitly. The decomposition of the entire diffusion term into two components is to more efficiently facilitate implementation of the fractional step method. Essentially, $D_\xi(u^\xi)$ contains terms similar to $\partial^2 u^\xi / \partial \xi^2 + \partial^2 u^\xi / \partial \eta^2 + \partial^2 u^\xi / \partial z^2$, while $D_{\xi,ex}$ contains the rest of the diffusion terms, those depending on the cross derivatives.

The explicit portion of the time advance is achieved using second-order Adams-Bashforth for the convection terms,

$$H_\xi(u^q) = \frac{3}{2} H_\xi(u^q)^n - \frac{1}{2} H_\xi(u^q)^{n-1}, \quad (42)$$

the pressure term advanced using implicit Euler,

$$R_\xi(P) = R_\xi(P)^{n+1}, \quad (43)$$

and Crank-Nicholson for the implicit diffusion terms,

$$D_\xi(u^\xi) = \frac{1}{2}D_\xi(u^\xi)^{n+1} + \frac{1}{2}D_\xi(u^\xi)^n, \quad (44)$$

and second-order explicit Adams-Bashforth scheme for the explicit diffusion terms,

$$D_{\xi,ex}(u^q) = \frac{3}{2}D_{\xi,ex}(u^q)^n - \frac{1}{2}D_{\xi,ex}(u^q)^{n-1} \quad (45)$$

Finally, the temporal discretization of (40) can be written for the three components of the momentum equation as,

$$\begin{aligned} V_\xi \frac{(u^\xi)^{n+1} - (u^\xi)^n}{\Delta t} &= \frac{1}{2}[3H_\xi(u^q)^n - H_\xi(u^q)^{n-1}] + R_\xi(P^{n+1}) \\ &+ \frac{1}{2}[3D_{\xi,ex}(u^q)^n - D_{\xi,ex}(u^q)^{n-1}] + \frac{1}{2}[D_\xi(u^\xi)^{n+1} + D_\xi(u^\xi)^n], \end{aligned} \quad (46)$$

$$\begin{aligned} V_\eta \frac{(u^\eta)^{n+1} - (u^\eta)^n}{\Delta t} &= \frac{1}{2}[3H_\eta(u^q)^n - H_\eta(u^q)^{n-1}] + R_\eta(P^{n+1}) \\ &+ \frac{1}{2}[3D_{\eta,ex}(u^q)^n - D_{\eta,ex}(u^q)^{n-1}] + \frac{1}{2}[D_\eta(u^\eta)^{n+1} + D_\eta(u^\eta)^n], \end{aligned} \quad (47)$$

$$\begin{aligned} V_z \frac{(u^z)^{n+1} - (u^z)^n}{\Delta t} &= \frac{1}{2}[3H_z(u^q)^n - H_z(u^q)^{n-1}] + R_z(P^{n+1}) \\ &+ \frac{1}{2}[3D_{z,ex}(u^z)^n - D_{z,ex}(u^z)^{n-1}] + \frac{1}{2}[D_z(u^z)^{n+1} + D_z(u^z)^n]. \end{aligned} \quad (48)$$

Summary of the fractional step method

The system (31) and (46)-(48) is solved using a fractional step method, comprised of three sequential operations: computation of a provisional velocity field using the non-linear and viscous terms; calculation of the pressure field by solving the Poisson equation, and finally projection of the intermediate velocity field onto a divergence-free space at the new time step using the pressure gradient. Written in a compact form, the series of operations are

$$A\hat{\mathbf{u}} = \mathbf{rhs} + \mathbf{mbc} \quad (49)$$

$$\Delta t D G \phi^{n+1} = D\hat{\mathbf{u}} - \mathbf{cbc} \quad (50)$$

$$\bar{\mathbf{u}}^{n+1} = \hat{\mathbf{u}} - \Delta t G \phi^{n+1} \quad (51)$$

where the G submatrix is the discrete gradient operator and D is the discrete divergence operator. The exact expressions for the coefficient submatrix A and right-hand-side submatrix \mathbf{r} are

dependent on the specific temporal and spatial discretizations. The unknown discrete velocity and pressure vectors are denoted $\bar{\mathbf{u}}^{n+1}$ and p^{n+1} . Boundary condition vectors \mathbf{mbc} and \mathbf{cbc} are defined such that when combined with operators G and D the original system with appropriate boundary conditions can be fully recovered.

Given the transformation to a general curvilinear system as outlined above, the fractional step method as implemented takes the form for the volume fluxes as,

$$A\hat{\mathbf{u}}^q = (\mathbf{S}^\xi, \mathbf{S}^\eta, \mathbf{S}^z)^T \cdot \mathbf{rhs} + (\mathbf{S}^\xi, \mathbf{S}^\eta, \mathbf{S}^z)^T \cdot \mathbf{mbc} \quad (52)$$

$$(\mathbf{S}^\xi, \mathbf{S}^\eta, \mathbf{S}^z)^T \cdot \Delta t D G \phi^{n+1} = D\hat{\mathbf{u}}^q - (\mathbf{S}^\xi, \mathbf{S}^\eta, \mathbf{S}^z)^T \cdot \mathbf{cbc} \quad (53)$$

$$\mathbf{u}^{q^{n+1}} = \hat{\mathbf{u}}^q - (\mathbf{S}^\xi, \mathbf{S}^\eta, \mathbf{S}^z)^T \cdot \Delta t G \phi^{n+1} \quad (54)$$

where the T superscript denotes the transpose. The vector of volume fluxes \mathbf{u}^q is the contravariant component of $\bar{\mathbf{u}}$ in the coordinate system defined by \mathbf{S}^q and \mathbf{S}_q .

3.2.2 Compressible flow solver

Solutions of the compressible Navier-Stokes equations are obtained using Cobalt₆₀, an unstructured finite-volume method developed for solution of the compressible Navier-Stokes equations and described in Strang *et al.* (1999). The governing equations for a compressible flow written in integral form are expressed as,

$$\frac{\partial}{\partial t} \iiint_{\mathcal{V}} Q d\mathcal{V} + \iint_{\mathcal{S}} (f\hat{\mathbf{i}} + g\hat{\mathbf{j}} + h\hat{\mathbf{k}}) \cdot \hat{\mathbf{n}} d\mathcal{S} = \iint_{\mathcal{S}} (r\hat{\mathbf{i}} + s\hat{\mathbf{j}} + t\hat{\mathbf{k}}) \cdot \hat{\mathbf{n}} d\mathcal{S}, \quad (55)$$

where,

$$Q = \begin{bmatrix} \rho \\ \rho u \\ \rho v \\ \rho w \\ \rho e \end{bmatrix} \quad f = \begin{bmatrix} \rho u \\ \rho u^2 + p \\ \rho uv \\ \rho uw \\ u(\rho e + p) \end{bmatrix} \quad g = \begin{bmatrix} \rho v \\ \rho uv \\ \rho v^2 + p \\ \rho vw \\ v(\rho e + p) \end{bmatrix} \quad h = \begin{bmatrix} \rho w \\ \rho uw \\ \rho vw \\ \rho w^2 + p \\ w(\rho e + p) \end{bmatrix} \quad (56)$$

$$r = \begin{bmatrix} 0 \\ \tau_{xx} \\ \tau_{xy} \\ \tau_{xz} \\ a \end{bmatrix} \quad s = \begin{bmatrix} 0 \\ \tau_{xy} \\ \tau_{yy} \\ \tau_{yz} \\ b \end{bmatrix} \quad t = \begin{bmatrix} 0 \\ \tau_{xz} \\ \tau_{yz} \\ \tau_{zz} \\ c \end{bmatrix}. \quad (57)$$

In the above, $a = u\tau_{xx} + v\tau_{xy} + w\tau_{xz} + kT_x$, $b = u\tau_{xy} + v\tau_{yy} + w\tau_{yz} + kT_y$, and $c = u\tau_{xz} + v\tau_{yz} + w\tau_{zz} + kT_z$. A fluid element volume over which the equations are enforced is denoted \mathcal{V} ; the bounding surface as \mathcal{S} with outward-pointing unit normal $\hat{\mathbf{n}}$. The Cartesian unit vectors are $\hat{\mathbf{i}}$, $\hat{\mathbf{j}}$, and $\hat{\mathbf{k}}$. The fluid density is denoted ρ , p is the pressure; u , v , and w are the velocity components; e is the specific energy per unit volume; T is the temperature; k is the thermal conductivity; and τ_{xx} , τ_{yy} , τ_{zz} , τ_{xy} , τ_{xz} , and τ_{yz} are the viscous stress tensor components. The ideal gas law closes

the system of equations and the entire equation set is non-dimensionalized by freestream density and speed of sound.

Integrating the equations around finite volumes in the domain leads to the semi-discrete form for the system,

$$\nu_i \frac{dQ_i}{dt} + \sum_{M=1}^{N_i} (f^M \hat{i} + g^M \hat{j} + h^M \hat{k}) \cdot \hat{n}^M S^M = \sum_{M=1}^{N_i} (r^M \hat{i} + s^M \hat{j} + t^M \hat{k}) \cdot \hat{n}^M S^M, \quad (58)$$

where the subscripted i and superscripted M denote quantities for the i^{th} cell and the M^{th} face of cell i , respectively, and N_i is the number of faces bounding cell i . The equations above can be solved on arbitrary cell types in Cobalt₆₀ (e.g., hexahedrals, prisms, tetrahedrons). The spatial operator uses the exact Reimann solver of Gottlieb and Groth (1988), least squares gradient calculations using QR factorization to provide second order accuracy in space, and TVD flux limiters to limit extremes at cell faces. A point implicit method using analytic first-order inviscid and viscous Jacobians is used for advancement of the discretized system. For time-accurate computations, a Newton sub-iteration scheme is employed, the method is second order accurate in time. Additional details on the method can be found in Strang *et al.* (1999).

For simulation of turbulent flows, an averaged set of the above equations are considered, this process leading to turbulent stresses that must be modeled in terms of other variables. A Boussinesq approximation is invoked in the momentum equations and the turbulent eddy viscosity, μ_t , is used to relate the stresses to the strain rate. The turbulent heat flux is also modeled using a gradient-transport hypothesis, requiring specification of a turbulent thermal conductivity k_t . Reynolds analogy is applied and the turbulent heat flux is modeled using a constant turbulent Prandtl number, $Pr_t = (c_p \mu_t) / k_t$, of 0.9. Using turbulent eddy viscosity and turbulent conductivity, the variable μ is replaced by $(\mu + \mu_t)$ and k is replaced by $(k + k_t)$ in the governing equations.

For parallel performance, Cobalt₆₀ uses the domain decomposition library ParMETIS (Karypis *et al.* 1997) to provide nearly perfect load balancing with a minimal surface interface between zones. Communication between processors is achieved using Message Passing Interface (MPI), with parallel efficiencies above 95% on as many as 1024 processors (see also Grismer *et al.* 1998).

3.3 Flow configuration and simulation design

In the first part of the study, two-dimensional computations of the flow around canonical forebody cross-sections were performed: a rounded-corner square and a 2:1 ellipse. Views of both cross sections for the two-dimensional computations are shown in Figure 2. For the rounded-corner square, the radius is 1/4 of the width/height ("diameter", D) of the forebody, similar to the cross-sections of the X-29 and T-38. With reference to Figure 2, the flow is at angle of attack α of 10° to the horizontal (x) axis. This is the angle of attack in the idealized two-dimensional problem, not the angle of attack of the airplane. In simplest terms, the computation emulates that of an

forebody at 90° angle of attack (an exactly flat spin), and rotating. The angle of attack here is then the arctangent of the ratio $\Omega D/V$ where Ω is the spin rate, D the distance from the nose to center of rotation of the spin, and V its sink velocity.

For the three-dimensional computations the numerical predictions of the flow over the rounded-corner square are compared to the experimental measurements from Polhamus *et al.* (1959). These investigators measured the forces and pressure distributions on a variety of forebody cross-sections over a range of Reynolds numbers and angles of attack, showing that there are important Reynolds number effects in the flow around forebodies at angle of attack. In the sub-critical regime (Reynolds numbers below about 5×10^5), boundary layer separation along the top surface of the rounded-corner square (upper-most horizontal surface in Figure 2a) occurs near the upper-front corner of the forebody, while for the super-critical flows the boundary layer remains attached along the lower and upper surfaces. For the ellipse the change in separation type is less pronounced given the configuration, with turbulent separation slightly aft of the upper shoulder and laminar boundary layer separation upstream of the upper shoulder of the model. The changes in boundary layer separation characteristics have significant effects on the streamwise and lateral forces with Reynolds number (the lateral, or side, force acts along the y axis in Figure 2). A reversal of the lateral force was measured in the experiments, i.e., negative for sub-critical flows and positive in the super-critical regime (for reference, the force is positive for an airfoil). Relevant to spin, the negative side force in the sub-critical regime is spin-propelling, while at the higher Reynolds numbers the positive side force is spin-damping.

The effects measured by Polhamus *et al.* (1959) are analogous to that of the drag crisis occurring around cylinders and spheres and are linked to boundary layer transition and the nature of the flow separation. While predicting details of the transition process is beyond the scope of the methods used in the current simulations, it is possible to construct well-defined computations to investigate the effect of the type of boundary layer separation on the flow. In particular, simulations were performed in the sub- and super-critical regimes in which the type of boundary layer separation was controlled via the initial and boundary conditions on the eddy viscosity.

Following, Travin *et al.* (2001), a 'tripless' approach is employed for sub-critical flows in which the inflow eddy viscosity is zero. Non-zero values are seeded into the wake and the reversed flow that is established in the recirculating region is sufficient to sustain the turbulence model downstream of separation. Boundary layer separation in this case is laminar, with the model active following separation. For the super-critical flows the inflow eddy viscosity is set to a small value (3ν), sufficient to ignite the turbulence model near solid surfaces as the fluid enters the boundary layers. The subsequent separation is then of a turbulent boundary layer.

Computations of the two-dimensional configurations presented below were performed using structured grids, most of the calculations of the three-dimensional flow were also performed on structured meshes. Structured grids were generated using the control technique of Hsu and Lee

(1991). Using this technique, it was possible to control mesh spacing to the first point nearest the boundary (within one wall unit near solid surfaces), exert control over grid spacing tangential to the boundary, and also to maintain orthogonality of the mesh at all boundaries. Important to the application of DES as a tool for predicting the flow around complex configurations is application of the method on unstructured grids. For the three-dimensional computations, DES predictions obtained on an unstructured mesh were also evaluated against experimental measurements and results from the structured grids. The unstructured grid was generated using Gridgen (Steinbrenner *et al.* 2000), with prisms in the boundary layer and near-isotropic tetrahedra away from solid surfaces.

Calculations of the three-dimensional flow around the forebody cross section were performed using both structured and unstructured grids. The unstructured grids are comprised of a combination of tetrahedra and prisms, while the structured grids are comprised of hexahedra. Prisms are used in the boundary layer in order to reduce the number of cells as well as to improve the efficiency of the boundary layer solution. Boundary-layer grids comprised of tetrahedra often possess high aspect ratios and can be strongly non-orthogonal. This presents problems in calculation of the divergence of the gradient. Prisms are more orthogonal and place less burden on the solver.

Finally, as also discussed above, one of the main objectives of the work are to understand forebody spin characteristics as they relate to side-force reversal and to assess/advance DES as a viable method for prediction of unsteady flows at high Reynolds numbers. The stability of DES results with changes in grid spacing is investigated, as well as other factors such as the dimension of the (statistically homogeneous) spanwise coordinate. DES results are also compared to predictions obtained from the unsteady Reynolds-averaged Navier-Stokes (URANS) equations (of both the two- and three-dimensional equations) and to simulations performed without an explicit turbulence model. The runs without a turbulence model are denoted as MILES (Monotone Integrated Large Eddy Simulation) to provide a link with relevant literature, although no detailed investigations were undertaken to evaluate the numerical dissipation in the current calculations and its role as an SGS model, and the numerical schemes are not monotone in a strict sense (see Fureby and Grinstein 1999 for a discussion of the MILES approach).

4 Results

4.1 Two-dimensional computations – URANS

The initial phase of the work was undertaken to develop and build confidence in the approach used to specify and control the type of boundary layer transition, i.e., either fully turbulent boundary layer separation or the triplex approach used for cases with laminar boundary layer separation. Unsteady RANS comprised the primary simulation technique for this stage of the work, the S-A model was employed to compute the eddy viscosity used to close the Reynolds stresses. The numerical solutions were of the unsteady incompressible flow using the fractional step method

outlined in §3.2.1. This portion of the study also enabled implementation and testing of the grid control strategy developed by Hsu and Lee (1991) for generation of structured meshes about the forebodies. A grid generation procedure was developed and tested for two canonical forebody cross-sections described above: a rounded-corner square and a 2:1 ellipse. Shown in Figures 2-4 are views of each geometry. In Figure 3 and Figure 4 show the grid and entire computational domain (frame *a* of each figure), a view in the vicinity of the forebody is also shown (frame *b* of each figure).

Important in application of the S-A model for URANS, as well as in the DES predictions presented in the next section, is resolution of the wall layer, i.e., the first grid point nearest a solid surface is located approximately one viscous unit from the surface with geometric stretching applied in the boundary layer. The stretching rate applied to the boundary layer grids were in the range 1.2 – 1.3, with the higher value representing a very aggressive stretching. The position of the first wall-normal grid point y_1^+ is estimated via,

$$y_1^+ = \frac{y_1 u_\tau}{\nu}, \quad u_\tau = \sqrt{\frac{\tau_w}{\rho}}, \quad (59)$$

where τ_w is the wall stress and related to the skin friction via $C_f = 2\tau_w/(\rho U_\infty^2)$. The above expression can be rewritten in terms of the skin friction coefficient C_f ,

$$y_1^+ = \frac{y_1}{D} \sqrt{\frac{C_f}{2}} Re_D, \quad (60)$$

where D is the body width/diameter and $Re_D = U_\infty D/\nu$. An estimate of y_1 corresponding to a viscous spacing approximately one wall unit can be obtained using a representative value of C_f , e.g, in the range $C_f \approx 0.002 - 0.004$, the higher value yielding a more conservative estimate of the near-wall spacing to the first point. For $y_1^+ = 1$, the formula (60) yields y_1/D in the range 10^{-5} for the Reynolds numbers considered in this work, Re_D on the order $10^5 - 10^6$.

For the rounded-corner square, Figure 3 shows the axial distance of the inlet from the front of the forebody is $3.5D$, the downstream extent $7.5D$, with the lateral dimension extending $3.5D$ at the maximum distance from the forebody. The domain for the 2:1 ellipse is similar, i.e., using the long axis as the characteristic length, the streamwise coordinate ranges $-4D \leq x \leq 8D$, the lateral dimension $-4D \leq y \leq 4D$. Figure 3b and Figure 4b show that near the forebody surface, the wall-normal grids are clustered, in the surface-tangent dimension the grids are shaded towards the wake with a higher density of cells in the aft region. Control of these features in the grid are relatively straightforward to achieve using the approach developed by Hsu and Lee (1991), a further advantage being the relatively low cell skewness. Grid refinement was carried out using simulations in which the surface-normal coordinate was refined from 100 to 150 points, the surface-tangential dimension was refined from 150 to 200 points.

Calculations of the two-dimensional configurations were performed for Reynolds numbers of 5×10^4 and 8×10^5 . The lower Reynolds number was employed for the initial investigations of

the tripless characteristics of the model, simulations at this Reynolds number lowering the computational burden (e.g., allowing slightly coarser meshes) and also alleviating difficulties initially encountered with the tripless approach. Eddy viscosity levels were observed to “creep” upstream of separation due to numerical errors, this aspect necessitating the modification to the production term using f_{v3} as described in §3.1. An example of the influence of boundary layer separation on the nature of the solution along the top surface of the rounded-corner square is shown in Figure 5. Both frames of the figure show instantaneous velocity vectors colored by the eddy viscosity ratio ν_t/ν . The computations corresponding to each frame were performed $Re_D = 5 \times 10^4$, in Figure 5a, the boundary layers on the forebody surface are fully turbulent, this feature accomplished by seeding the inlet plane with a small level of eddy viscosity, $\nu_t/\nu = 3$. This level of eddy viscosity is sufficient to activate the turbulence model in the boundary layers, a consequence and illustrated in Figure 5a is that the boundary layers possess sufficient momentum to withstand the adverse pressure encountered as the flow develops along the top surface of the forebody. Consequently, boundary layer separation is delayed, occurring near the upper rear corner as shown in the figure. Figure 5b shows instantaneous velocity vectors from the tripless solution. The tripless solution is created by seeding the initial flow with eddy viscosity and with zero eddy viscosity prescribed at the inlet to the computational domain. The reverse flow region sustains the model, Figure 5b shows that boundary layer separation occurs near the upper front corner of the forebody. In this case, the boundary layers developing along the forebody are effectively laminar and do not possess sufficient momentum to withstand the adverse pressure gradient that develops as the flow progresses around the upper front corner and along the top surface. The larger region of non-zero eddy viscosity (red vectors in the figure) is due to the separation, the recirculating region that has developed along the upper surface sweeping eddy viscosity into the regions above the forebody. Importantly for this case, the turbulence model remains dormant in the region upstream of separation.

Variations in the pressure coefficient, skin friction, and “turbulence index” around the perimeter of the 2:1 ellipse are shown in Figure 6. The distributions are shown for a tripless solution at $Re_D = 5 \times 10^4$ in Figure 6a and a case with fully turbulent boundary layers at $Re_D = 8 \times 10^5$ in Figure 6b. The horizontal coordinate defines the angle around the perimeter and is measured positive in the clockwise direction. The coordinates $\theta = 0$ and 360 degrees correspond to the windward symmetry point, the upper and lower “shoulders” of the ellipse coinciding with $\theta = 90$ and 270 degrees (where the potential flow at 0 degrees angle of attack would possess the minimum pressure). The pressure coefficient distribution in both Figure 6a and Figure 6b possess common features on the front of the body, the stagnation pressure is predicted near $\theta = 0$ and there is a relatively rapid decrease as the flow accelerates around the upper and lower shoulders of the ellipse. The back pressure for the case with laminar separation in Figure 6a shows larger suction, an effect that will lead to a larger axial force. The skin friction distribution for both cases shows the zero crossing marking the location of flow separation. For the 2:1 ellipse, separation for the two

cases occurs at similar angles, only slightly delayed for the fully turbulent case around the lower corner, occurring at nearly the same angle around the upper corner. For both the tripless and fully turbulent solutions, C_f increases as the flow accelerates towards the upper and lower shoulders and then is nearly zero in the separated region.

Also shown in the figure is the “turbulence index”, which defines the position at which the turbulence model becomes active. For the S-A model, the turbulence index is defined as,

$$i_t = \frac{1}{\kappa} u_\tau \frac{\partial \tilde{\nu}}{\partial n}, \quad (61)$$

where the coordinate n defines the surface normal. The index is zero in a laminar region, followed by a sharp increase in the “transition region”, i.e., the region over which the model becomes active, and then remains around unity or takes on higher values in the fully turbulent regions. Figure 6a shows that for the tripless case the abrupt increase in the turbulence index coincides with the zero crossing in the skin friction, i.e., with boundary layer separation, in turn showing the tripless character of the solution in that the model remains dormant in the attached boundary layer upstream of separation. Figure 6b shows that for the fully turbulent boundary layers the turbulence index is essentially equal to unity prior to separation, abruptly increasing as the flow separates (the sharp increase due to small/zero values in u_τ).

An example of the unsteady character of the URANS solution is illustrated for the rounded-corner square in Figure 7. Shown are vorticity contours for several phases of the motion through roughly one shedding cycle. The calculations are from a fully turbulent case at $Re_D = 8 \times 10^5$ for which the turbulent boundary layers separate near the upper and lower surfaces of the model, an effect observed in the contours. The vorticity contours show essentially a periodic shedding, with well organized structures developing in the wake, the figure also showing that the asymmetry that develops in the wake due to the 10° angle of attack of the freestream. The distributions of the pressure coefficient, skin friction, and turbulence index corresponding to the frames shown in Figure 7 are shown in Figure 8. As observed earlier for the ellipse, the turbulence index is approximately equal to one in the attached boundary layers upstream of separation, sharply rising following flow detachment. Zero crossings in the skin friction again identify the separation location. For the fully turbulent solution, Figure 7 shows that separation occurs near the rear of the upper and lower horizontal surfaces, corresponding to angles $\theta \approx 130^\circ$ (top surface) and $\theta \approx 230^\circ$ (bottom surface). For all of the phases of the shedding, the pressure coefficient distribution shows that there is a very large acceleration as the flow negotiates the upper front corner, the deep decrease in C_p occurring because the boundary layer remains attached through this region. A smaller minima in C_p occurs near the lower front corner ($\theta \approx 315^\circ$) due to boundary layer acceleration. The skin friction distribution shows that there is no boundary layer separation along the lower horizontal surface. A clearly observed effect of vortex shedding is the change in the pressure distribution along the rear surface of the forebody, for $130 \leq \theta \leq 225$ degrees. Figure 8a,

Case	Model	Grid Size	L_z	x - y domain
1	DES	$100 \times 149 \times 151$	$3D$	baseline
2	DES	$100 \times 149 \times 301$	$6D$	baseline
3	DES	$150 \times 200 \times 151$	$3D$	baseline
4	DES	$120 \times 149 \times 151$	$3D$	padded
5	DES	unstructured, 3.55×10^6 cells	$3D$	padded
6	MILES	$120 \times 149 \times 151$	$3D$	padded
7	URANS	200×400	–	baseline
8	URANS	$120 \times 149 \times 151$	$3D$	padded

Table 1: Simulation parameters. Grid size reported as surface-normal \times surface-tangential \times spanwise; “baseline” is the smaller x - y domain, “padded” the larger x - y domain. URANS calculations performed using the Spalart-Allmaras one-equation model.

for example shows a relatively large suction along the rear vertical surface, the corresponding flow visualization in Figure 7a shows a vortex rolling up directly behind the rear vertical surface.

4.2 Three-dimensional computations – DES and URANS

In the first part of the study the tripless approach to producing solutions undergoing laminar boundary layer separation and with a turbulent wake were developed and tested. Overall, the behavior of the approach is well-defined, not sensitive to initial or boundary conditions, etc. In the second phase of the work, three-dimensional computations of the flow around the forebody were performed, a schematic of the geometry and indication of the angle of the incident flow is shown in Figure 9 for convenience.

The parameters of the three-dimensional calculations are summarized in Table 1. Shown is the case number, model, grid size, spanwise period, and reference to the x - y domain size. Assessment of unstructured approaches to eddy-resolving calculations is enabled via Case 5, the ability to exert greater control on cell distribution compared to the structured grids permitted generation of an unstructured mesh having 2.5×10^6 cells (of a total cell size of 3.55×10^6 cells) within two diameters of the model surface.

The majority of simulations were performed on domains in which the spanwise dimension was three times the diameter, i.e., $L_z = 3D$. The influence of the spanwise period was investigated in Case 2 via computations performed on a domain with a doubling of the spanwise period to $L_z = 6$. Domain-size influences were also investigated in calculations with two domains having different outer-boundary placement. The smaller domain (referred to as “baseline” in the table) extended eight diameters downstream of the body and with a lateral extent also of $8D$, a projection of the grid onto the x - y plane for the baseline configuration is shown in Figure 10.

In calculations performed on the larger domains (referred to as “padded” in the table), the

streamwise extent to the outflow boundary downstream of the body was at approximately $20D$, with the lateral dimension also approximately $20D$ from the model surface. As shown in the next section, there was a measurable effect of the baseline domain on the solutions, resulting in over-predictions of the stagnation pressure and axial force. Boundary conditions on the model surface were no-slip for the velocity components and turbulent viscosity. The normal momentum equation is used at solid walls to estimate the variation of pressure normal to the surface, while a one-sided, least-squares gradient method is used to estimate the variation of pressure tangential to the wall.

Grid resolution effects were investigated by refining the mesh in the x - y plane by a factor of two. For the coarse grid with the shorter spanwise dimension ($L_z = 3D$), the structured-grid calculation was performed using approximately 2.2×10^6 points, the finer mesh calculation possessing about 4.5×10^6 grid points. Because Δ in (12) near the surface was set by the spanwise spacing, the thickness of the “RANS region”, i.e., the dimension from the model surface to the interface at which \tilde{d} is set by the grid spacing for all the DES runs was $0.013D$. The dimensionless timestep, $\Delta t/(D/U_\infty)$ (U_∞ is the freestream speed), was 0.01, a conservative value chosen based on preliminary calculations and previous time-accurate computations of unsteady flows by the current investigators and other researchers (e.g., see Travin *et al.* 2001). With $\Delta t/(D/U_\infty) = 0.01$, there are approximately 350 timesteps per main shedding cycle.

From a given set of initial and boundary conditions for a particular flow type (tripless or fully-turbulent), the governing equations were time advanced through a transient as the flow evolved to its equilibrium condition. This transient, typically less than $20D/U_\infty$, was discarded and the simulations continued for an additional period of $\mathcal{O}(100D/U_\infty)$. This period was sufficient for adequate convergence of averaged quantities and capture of the long timescales in the flow. Initial perturbations supplied to the flow triggered the breakdown in the wake and development of three-dimensional structures.

A snapshot of the instantaneous velocity vectors in a plane near the upper rear corner (θ in the range 135°) for a turbulent separation run (Case 4) is shown in Figure 11. The interface beyond which \tilde{d} is set by the grid has been drawn. The figure shows a smooth transition between the “RANS region” and “LES region” of the solution with essentially all of the boundary layer within the RANS region. In addition, the outer part of the boundary layer has very little sensitivity to the destruction term of the S-A model, the only one that changes between RANS and LES modes.

The different structure of the sub- and super-critical flows is illustrated in Figure 12. For the sub-critical flow at $Re = 10^5$ the attached boundary layers are laminar and cannot sustain the development of the adverse pressure gradient in the upper front corner with separation occurring around $\theta \approx 45^\circ$. In the “tripless” mode, the turbulence model is dormant upstream of separation, with flow reversal sustaining the model downstream of separation. Contrasted with Figure 12b, the tripless case exhibits massive separation along the upper surface, the fully turbulent solution in Figure 12b shows the influence of the fully turbulent boundary layers along the forebody, in

particular the attached flow along the top surface with separation towards the rear. Both flows show that the wake is chaotic and three-dimensional.

Shown in Figure 13 are a representative sample of pathlines in the vicinity of the upper front corner of the forebody for the flow at $Re = 10^5$ (Case 4 in Table 1). The pathlines in the figure are colored by the value of the viscosity ratio ν_t/ν . They cross in this view, because the flow is three-dimensional. Upstream of separation the eddy viscosity is zero (as indicated by the blue color of the pathline). In the separated region the reversing flow sweeps turbulent fluid from downstream into contact with the separating flow. Important to note is that there is not a “transition creep”, i.e., a numerical diffusion of non-zero eddy viscosity into regions upstream of separation.

In “natural” applications of DES, the detached regions of the flow are computed using LES, in this case with a one-equation model for the subgrid-scale eddy viscosity. An advantage of LES is that mesh refinement resolves more flow features, in turn lessening modeling errors and driving the solution towards the DNS limit. The effect of mesh refinement was investigated by doubling the x - y grid in Case 3 as compared to Case 1 (c.f., Table 1). Shown in Figure 14a and Figure 14b are instantaneous vorticity contours from Case 1 and Case 3, respectively, for a simulation with turbulent separation at $Re = 8 \times 10^5$. Cuts of the vorticity field from three spanwise planes are shown for each case and provide an example of the strong spanwise variation in the DES solution. As also the case for classical LES, Figure 14 shows that the effect of the mesh refinement is to resolve smaller-scale eddies in Case 3. This feature in the DES was also illustrated in the circular cylinder calculations of Travin *et al.* (2001).

Also shown in Figure 14 are vorticity contours in the forebody wake from solutions obtained using the unstructured grid (Case 5) and a triplex solution with simulation parameters corresponding to Case 3. The unstructured-grid prediction shows roughly a comparable range of eddies resolved in the wake as the fine-mesh result obtained for Case 3. That the unstructured result yields similar structure as Case 3 is significant since it demonstrates that unstructured meshes provide an efficient means for performing DES, the ability to exert a more local control on the mesh in the focus region in the wake of the body an important aspect for turbulence-resolving simulations. Vorticity contours from the triplex solution in Figure 14d show a substantially different structure than achieved in the fully turbulent solutions. Boundary layer separation is apparent near the upper front corner of the forebody, with a wider wake developing downstream. A zoomed view of the vorticity contours is shown in Figure 15 shows instantaneous vorticity contours in the wake for the fully turbulent solution from the structured-grid prediction (Case 3) and the unstructured-grid prediction (Case 5). Visually, the range of scales resolved in the wake is comparable for the two grids.

Force coefficients C_x and C_y in the axial and lateral directions, respectively, are defined using the freestream density and velocity and frontal area of the forebody. Figure 16 shows the force coefficient time histories for the two-dimensional URANS solution at $Re = 8 \times 10^5$. A fraction of

the time history is shown in the figure, i.e., following the initial transient. The figure shows the 2D URANS solution is temporally periodic, with large swings in the side force coefficient compared to the axial value as the flow undergoes a shedding cycle.

A representative force coefficient history for a DES run is shown in Figure 16, for a turbulent separation run at $Re = 8 \times 10^5$ (Case 2). Similar to Figure 16, a transient of roughly 20 non-dimensional time units has been excluded from the figure (note also the longer time integration for the DES). Unlike the 2D URANS, a strong modulation is apparent in the side force coefficient C_y , similar to that observed in related studies of cylinders and other bluff bodies (e.g., see Travin *et al.* 2001). The side-force modulation is complex and seems to be an intrinsic feature of the chaotic, three-dimensional flow. For the forebody, the modulation develops via the interaction of spanwise and streamwise vorticity in the near wake. DES calculations on domains in which the spanwise coordinate L_z was $1.5D$ did not yield force modulation and suppressed three-dimensionality of the primary spanwise structure (although the solution possessed streamwise vorticity). Predictions on the domain with $L_z = 1.5D$ yielded large over-predictions of the axial force. Though not shown here, force-coefficient histories for all of the three-dimensional turbulent separation cases – including the 3D URANS result – exhibited force modulation.

Time-averaged force coefficients for the turbulent separation cases are summarized in Table 2. The 2D URANS, which produces a periodic shedding and cannot accurately account for the force modulation, substantially over-predicts the mean axial force coefficient $\langle C_x \rangle$. This feature is analogous to the circular cylinder where two-dimensional URANS yields large drag (Travin *et al.* 2001). For the DES, force coefficients from the smaller (baseline) domains are higher than the measured values and than those from calculations performed on the larger domain (c.f., Cases 1-3). A comparison of Case 3 against Cases 1-2 show a trend towards lower axial force with grid refinement in the x - y plane. In addition, the axial force slightly decreases in Case 2, computed on the longer spanwise domain, compared to Case 1. Nevertheless, $\langle C_x \rangle$ is too high and, as shown below, the over-prediction arises from the influence of the computational domain, which effectively constrains the flow and raises the stagnation pressure coefficient by about 0.1 compared to results obtained on the larger domains (Cases 4-5). DES predictions on the larger domain using both structured and unstructured grids are in quite good agreement with the measurements of Polhamus *et al.* (1959). Interestingly, the 3D URANS also yields forces in good agreement with the measurements and padded-domain DES predictions. On the other hand, calculations without an explicit turbulence model (Case 6) markedly over-predict the axial force due to the poor treatment of the attached boundary layers, as described in more detail below.

Pressure coefficients around the body for the fully-turbulent runs ($Re = 8 \times 10^5$) are shown in Figure 17. The angle θ is measured counter-clockwise from the aft-symmetry point of the forebody. For the flow at 10° angle of attack, the maximum C_p occurs about $15 - 20^\circ$ below the fore-symmetry point ($\theta \approx -160^\circ$ as shown in Figure 17). For Cases 1, 3, and 7, the stagnation

Case	Model	$\langle C_x \rangle$	$\langle C_y \rangle$
1	DES	0.57	0.92
2	DES	0.55	0.98
3	DES	0.51	0.96
4	DES	0.46	0.94
5	DES	0.43	0.83
6	MILES	0.76	0.62
7	2D URANS	0.75	0.88
8	3D URANS	0.43	0.94
–	expts.	0.4	0.9

Table 2: Time-average force coefficients from turbulent separation cases at $Re = 8 \times 10^5$ (time averages denoted using $\langle \cdot \rangle$). Experimental measurements are from Polhamus *et al.* (1959).

C_p is over-predicted, an error introduced by the use of the smaller x - y domain. For these cases the over-prediction in the stagnation pressure is $\mathcal{O}(0.1)$, comparable to the over-prediction of the mean axial force (c.f., Table 2). Comparing the effect of the domain (Case 1 and Case 4) shows a reduction in the axial force coefficient on the larger domain, closer to the measured value of about 0.4 as also summarized in Table 2. The 2D URANS, with a finer x - y grid compared to the three-dimensional runs also shows deeper minima in C_p in the vicinity of each corner, providing some insight into the effect of grid resolution on the pressure field.

An effect of the Reynolds number reproduced in the fully-turbulent solutions in Figure 17 is that the boundary layers around the upper front and lower front corners ($\theta \approx \pm 135^\circ$) remain attached, as evidenced by the strong pressure minima in these regions, especially around $\theta \approx 135^\circ$. It is apparent that all of the simulations predict attached boundary layers around the upper front corner, with the exception of the MILES run (Case 6), i.e., the simulation performed without an explicit turbulence model in which the (laminar) boundary layer separates. Accurate prediction of boundary layer growth and separation in MILES requires the boundary layer grid be sufficiently fine to resolve the small near-wall turbulent structures (as would also be required in whole-domain LES with an explicit SGS model). In practice, however, boundary layer grids will not be sufficiently dense for high Reynolds numbers flows because of the high computational cost. In the present case, the resulting MILES boundary layer prediction lacks turbulent structures and is essentially laminar.

Along the rear vertical surface (in the vicinity $\theta = 0$ in Figure 17) the 2D URANS (Case 7) pressure distribution is far from the measured values, resulting in a large streamwise force (c.f., Table 2) as also observed in other two-dimensional URANS predictions of bluff-body flows (e.g., see Travin *et al.* 2001). For all other cases shown in the figure, including the 3D URANS, predictions of the rear-surface pressures are reasonable, close to the measurements of Polhamus *et al.* (1959). Consequently, for the DES and 3D URANS calculations on the padded domains (Cases 4, 5, and

8), the overall pressure distributions are adequate and the axial and streamwise forces exhibit reasonable agreement with measurements. The accuracy of the 3D URANS result is surprising since flow visualizations show the solution lacks the streamwise vorticity apparent in the DES predictions shown in Figure 12. Flow visualizations show that the 3D URANS solution exhibits weak, but persistent, three-dimensionality in the primary spanwise vorticity shed from the forebody. Because the peak suction is missed in the MILES run (Case 6), the axial force is too high, yielding a similar $\langle C_x \rangle$ to the 2D URANS, though the causes for the over-predictions by these two techniques are not the same.

Mean side-force coefficients summarized in Table 2 show that the DES predictions of the lateral force coefficient $\langle C_y \rangle$ are in general not far from the measurements reported by Polhamus *et al.* (1959). The lateral force prediction in the MILES case provides another illustration of the error that can arise due to the boundary layer treatment in this technique. As also noted in the C_p distribution and axial force coefficient, the 3D URANS is again accurate and apparently able to resolve enough of the 3D variation important to accurate force predictions.

Laminar separation cases in the DES were computed for most of the parameter combinations summarized in Table 1. The Reynolds number in the laminar separation runs was 1×10^5 for the DES (4×10^5 for the 2D URANS shown below), well below the critical value found by Polhamus *et al.* (1959) of approximately 5×10^5 . In the tripless mode, the upstream eddy viscosity was zero. The wake was initially seeded with eddy viscosity and the reversing flow established behind the forebody is sufficient to sustain the turbulence model following separation.

A representative force history from a laminar separation case is shown in Figure 18. The simulation parameters for this case correspond to those of Case 4 in Table 1. As shown qualitatively via Figure 12, below the critical Reynolds number the flow separates in the vicinity of the upper front corner of the forebody. The measurements of Polhamus *et al.* (1959) indicate that the boundary layer along the lower surface of the forebody remains attached. The pressure distribution then develops lower pressures along the lower forebody surface compared to the upper surface, which has the result of reversing the magnitude of the side force as compared to the values measured at higher Reynolds numbers, past the critical value.

The force histories shown in Figure 18 show a higher axial force than in the fully turbulent runs. The mean axial force for this case is around 0.8, not far from the value reported in Table 2 for the MILES run at $Re = 8 \times 10^5$, which also experiences flow detachment in approximately the same region near the upper front corner. More importantly, the side force C_y in Figure 18, while chaotic, is only infrequently negative. Therefore, the mean side force will not be negative (the mean C_y is 0.38 for the trace in Figure 18) and the simulation does not yield a reversal in the magnitude of the side force. Changing the type of separation produces a very tangible move in the correct direction, but still an insufficient one.

The pressure coefficient distribution around the forebody for the laminar separation DES (Case 4

parameters) is shown along with the experimental measurements of Polhamus *et al.* (1959). For comparison, the C_p distribution from the 2D URANS calculation at $Re = 4 \times 10^5$ is also shown. Consistent with the flow visualization shown in Figure 12, flow detachment around $\theta \approx 135^\circ$ results in a substantially higher C_p compared to the turbulent separation case in Figure 17. Both the DES and 2D URANS have lower minima, indicative of delayed boundary layer separation as compared to the experiments. Near the lower front surface ($\theta \approx -135^\circ$), measurements show a deeper minimum than predicted in the DES. The 2D URANS, on the other hand, comes closer to predicting the pressure minima along the lower surface. Along the rear vertical surface ($\theta \approx 0^\circ$), DES predictions of the pressure distribution are reasonable. However, because of the deeper minima in the DES C_p near $\theta \approx 135^\circ$ and higher C_p along the lower flat surface, side force reversal cannot occur. Inspection of the instantaneous fields shows that along the lower flat surface (in the vicinity of $\theta \approx 135^\circ$), a thin region of reversed flow occurs in the DES (in the mean). This reversed flow region contributes to an effectively altered geometry that prevents development of a deep C_p minimum as apparently occurs in the experiments. To determine if the development of the thin region of reversed flow was caused by numerical and/or modeling errors, a Direct Numerical Simulation of the two-dimensional flow at $Re = 1 \times 10^4$ was conducted using a grid of 1600×1200 points. The DNS result shows a similar thin region of reversed flow along the lower surface of the forebody, near the lower front corner. Though not shown in Figure 19, the C_p distribution for the DNS is similar to the tripless DES prediction at $Re = 1 \times 10^5$.

5 Summary and Perspectives

DES was applied to prediction of the separated flow around an idealized jet-fighter forebody at 10° angle of attack. Influences of domain size, grid refinement, and turbulence model were investigated in cases in which boundary layer separation was either laminar, or turbulent. The initial and boundary conditions on eddy viscosity set the type of boundary-layer separation, aimed at flows above or below the critical Reynolds number which controls a reversal of the side force in the experimental measurements of Polhamus *et al.* (1959).

In general, DES predictions of the super-critical flow seem robust, tending towards experimental measurements with grid refinement, for example. The complex shedding process and modulation in the forces are consistent with circular-cylinder behavior and appear to be represented reasonably adequately, based on the agreement between simulation and measurement of the pressure distribution and forces. In the sub-critical regime, no simulation technique applied during the course of this study (DES/LES, DNS, and preliminary calculations using vortex methods) yielded a sign change in the side force. Small differences in the geometry, hysteresis, and sidewall effects are three sources that might explain the differences between predictions of the sub-critical flow and experimental measurements.

Aside from these effects, boundary layer treatment of the sub-critical flow may be simplistic, although fully "state-of-the-art". The advantage of the tripless approach is that the simulation parameters are unambiguous (the results depend only on the model, and not on transition locations chosen case by case). In practice, there can be substantial regions of laminar flow and a prediction of boundary layer transition is required. Details of the processes of separation and transition to turbulence as they inter-mingle continue to strongly challenge current modeling approaches.

In the present application, the attached boundary layers lie entirely within the "RANS region" of the DES solution. As the flow detaches, in the separating shear layers the wake develops new instabilities that result in the rapid growth of a chaotic and three-dimensional wake. The lack of eddy content in the detaching boundary layers represents a relatively small error to the solutions presented here (its length scale would be several times smaller than that of the new instabilities). In other applications, e.g., flows with shallow separations, it will be advantageous and necessary to seed the upstream flow with 'eddy content', considerably refine the grid to support these eddies, and initiate LES in the attached boundary layers prior to separation.

The current study also provided an opportunity to assess the solver and build confidence in the application of a second-order unstructured method for DES applications. The algorithm was sufficiently accurate to capture the growth of instabilities in the wake on both structured and unstructured grids of reasonable density. Streamwise vortices were captured with between five and ten cells in both cases. These features are connected to aspects of the numerical method, such as least-squares calculations of spatial derivatives and the use of non-linear dissipation (i.e., a TVD type limiter). Higher order methods should be expected to retain a given solution quality while reducing the number of cells required. However, obtaining higher order solutions on unstructured grids is significantly more challenging than on structured grids. Additionally, higher order methods would likely reduce the scalability of the algorithm. A side-by-side comparison to a higher-order numerical method would provide important estimates of potential benefits from a higher order of accuracy (and/or lower level of numerical dissipation), in turn allowing one to determine the trade-offs between various approaches. DES predictions on the unstructured grid showed the potential benefit of the unstructured approach in placing points precisely where they are needed – in the near wake. This study, however, is not a comprehensive testing of the numerics, since it only included experimental surface pressures for validation. More detailed comparisons, including wake profiles and spectra are needed to further assess the current approach.

The research reported as part of this undertaking and related efforts are increasing confidence in the use of Computational Fluid Dynamics as a more viable tool, capable of providing accurate predictions of unsteady flow in regimes which have been either very difficult to predict (using URANS) or pose too large a computational cost (using LES). Increasingly, many military aircraft are comprised of unusual configurations, e.g, AWACS-like antennas, joined wings, stealth shapes, etc. Given these disparate configurations, there is a pressing need for detailed information about

their aerodynamics that will be continue to pose significant problems for traditional testing based on wind-tunnel and flight tests. CFD is positioned to provide detailed predictions on timescales that will complement current efforts used for analysis and some engineering design.

Advances in DES currently depend both on the physical modeling, e.g., incorporation of roughness models, treatment of laminar-to-turbulent transition, as well as on numerical aspects such as grid generation, code performance for unsteady flow simulations, and issues related to factors such as numerical dissipation. Unstructured grids appear to hold great promise for complex configurations, a key finding of the present work was the similar, and accurate, prediction of the forces and pressures acting on the forebody in calculations using unstructured grids as compared to structured-grid results. This finding reinforces the importance of grid quality, e.g., low cell skewness, as the important factor for assessing quality, rather than simply whether the grid is unstructured or structured. For DES, guiding the grid, e.g., finely meshing the "focus region" where additional flow detail is crucial is relatively straightforward using unstructured grids. Further, with the continued development and application of adaptive gridding, the accuracy and fidelity of DES predictions should continue to improve.

References

- [1] Anderson, S.B., 1979, "Historical overview of stall/spin characteristics of general aviation aircraft", *J. Aircraft*, **16**(7), pp. 455-461.
- [2] Batten, P., Goldberg, U. and Chakravarthy, S., 2000, "Sub-grid turbulence modeling for unsteady flow with acoustic resonance", *AIAA Paper 00-0473*.
- [3] Bihrlé, W. Jr., Hultberg, R.S. & Mulcahy, W., 1978, "Rotary balance data for a typical single engine low-wing general aviation design for an angle-of-attack range of 30° to 90°", NASA CR 2972.
- [4] Constantinescu, G.S., Pacheo, R. and Squires, K.D., 2002, "Detached-Eddy Simulation of flow over a sphere", *AIAA Paper 2002-0425*.
- [5] Durand, W.F. (editor), *Aerodynamic theory: a general review of progress*, Springer, 1934-36.
- [6] Durbin, P.A., 1995, "Separated flow computations using the $k - \epsilon - v^2$ model", *AIAA J.*, **33**, p. 659.
- [7] Fritz, D., 1995, "An investigation into the use of two-dimensional Navier-Stokes computations to predict spin characteristics", report prepared under NASA contract NAS1-19672.
- [8] Fureby, C. and Grinstein, F.F., 1999, "Monotonically integrated large eddy simulation of free shear flows", *AIAA J.*, **37**, pp. 544-556.

- [9] Gottlieb, J.J. and Groth, C.P.T., 1988, "Assessment of Riemann Solvers for Unsteady One-Dimensional Inviscid Flows of Perfect Gases", *Journal of Computational Physics*, **78**, pp. 437-458.
- [10] Grismer, D.S. & Jenkins, J.E., 1997, "Critical-state transients for a rolling 65-degree delta wing", *J. Aircraft*, **34**(3), pp. 380-386.
- [11] Hsu, K. and Lee, S.L., 1991, "A Numerical Technique for Two-Dimensional Grid Generation with Grid Control at All of the Boundaries", *Journal of Computational Physics*, **11**, pp. 451-469.
- [12] Hultberg, R.S. & Mulcay, W., 1980, "Rotary balance data for a typical single engine general aviation design for an angle of attack range of 8° to 90°, I: low wing model A", NASA CR 3100.
- [13] Jenkins, J.E., Myatt, J.H. & Hanff, E.S., 1996, "Body-axis rolling motion critical states of a 65-degree delta wing", *J. Aircraft*, **33**(2), pp. 268-278.
- [14] Jenkins, J.E., 1997, "Nonlinear aerodynamic characteristics of a 65-degree delta wing in rolling motion: implications to testing and flight mechanics analysis", *AIAA Paper 97-0742*.
- [15] Jobe, C.E., Hsia, A.H., Jenkins, J.E. & Addington, G.A., 1996, "Critical states and flow structure on a 65-degree delta wing", *J. Aircraft*, **33**(2), pp. 347-352.
- [16] Karypis, G., Schloegel, K. and Kumar, V., "ParMETIS: Parallel Graph Partitioning and Sparse Matrix Ordering Library Version 1.0", University of Minnesota, Department of Computer Science, Minneapolis, MN 55455, July 1997.
- [17] McCormick, B.W., 1981, "Equilibrium spinning of a typical single-engine low-wing light aircraft", *J. Aircraft*, **18**(3).
- [18] Mittal, R. and Moin, P., 1997, "Suitability of Upwind-Biased Finite Difference Schemes for Large-Eddy Simulation of Turbulent Flows," *AIAA J.*, **35**(8), pp. 1415-1417.
- [19] Myatt, J.H., 1997, "Modeling the rolling 65-degree delta wing with critical state encounters", *AIAA Paper 97-3646*.
- [20] Nikitin, N.V., Nicoud, F., Wasistho, B., Squires, K.D. and Spalart, P.R., 2000, "An approach to wall modeling in Large-Eddy Simulation", *Phys. Fluids*, **12**, pp. 1629-1632.
- [21] Polhamus, E.C., Geller, E.W. and Grunwald, K.J., 1959, "Pressure and Force Characteristics of Noncircular Cylinders as Affected by Reynolds Number with a Method Included for Determining the Potential Flow about Arbitrary Shapes", NASA TR R-46.

- [22] Shur, M.L., Spalart, P.R., Strelets, M.K. and Travin, A.K., 1999, "Detached-Eddy Simulation of an Airfoil at High Angle of Attack," *Fourth International Symposium on Engineering Turbulence Modelling and Measurements*, Corsica, France.
- [23] Spalart, P.R. and Allmaras, S.R., 1994, "A One-Equation Turbulence Model for Aerodynamic Flows," *La Recherche Aerospatiale* **1**, pp. 5-21.
- [24] Spalart, P.R., Jou, W.H., Strelets, M. and Allmaras, S.R., 1997, "Comments on the Feasibility of LES for Wings, and on a Hybrid RANS/LES Approach," *First AFOSR International Conference on DNS/LES*, Rouston, Louisiana, USA.
- [25] Spalart, P.R., 2000, "Strategies for Turbulence Modeling and Simulations", *International Journal of Heat and Fluid Flow*, **21**, p. 252-263.
- [26] Speziale, C.G., 1998, "Turbulence modeling for time-dependent RANS and VLES: a review", *AIAA Journal*, **36**.
- [27] Steinbrenner, J., Wyman, N., Chawner, J., 2000, "Development and Implementation of Gridgen's Hyperbolic PDE and Extrusion Methods," *AIAA Paper 00-0679*.
- [28] Strang, W.Z., Tomaro, R.F, Grismer, M.J., 1999, "The Defining Methods of Cobalt₆₀: a Parallel, Implicit, Unstructured Euler/Navier-Stokes Flow Solver," *AIAA Paper 99-0786*.
- [29] Strelets, M., 2001, "Detached-Eddy Simulation of Massively Separated Flows", *AIAA Paper 2001-0879*.
- [30] Tischler, M.B. & Barlow, J.B., 1980, "Determination of the spin and recovery characteristics of a general aviation design", *J. Aircraft*, **18**, pp. 238-244.
- [31] Tobak, M. & Chapman, G.T., 1985, "Nonlinear problems in flight dynamics involving aerodynamic bifurcations", AGARD Symposium on Unsteady Aerodynamics – Fundamentals and Applications to Aircraft Dynamics, AGARD CP-386, Paper 25.
- [32] Travin, A., Shur, M., Strelets, M. and Spalart, P., 2001, "Detached-Eddy Simulations past a Circular Cylinder", *Flow, Turbulence and Combustion*, **63**, pp. 293-313.
- [33] Tromp, J.C., 1998, "Flow field simulation about a 65-degree delta wing during constant roll-rate motions", *AIAA Paper 98-4453*.
- [34] Troung, K.V. & Tobak, M., 1990, "Indicial response approach derived from Navier-Stokes equations: Part 1 - time-invariant equilibrium state", NASA TM-102856.
- [35] Von Terzi, D.A. and Fasel, H.F., 2002, "A new flow simulation methodology applied to the turbulent backward-facing step", *AIAA Paper 2002-0429*.

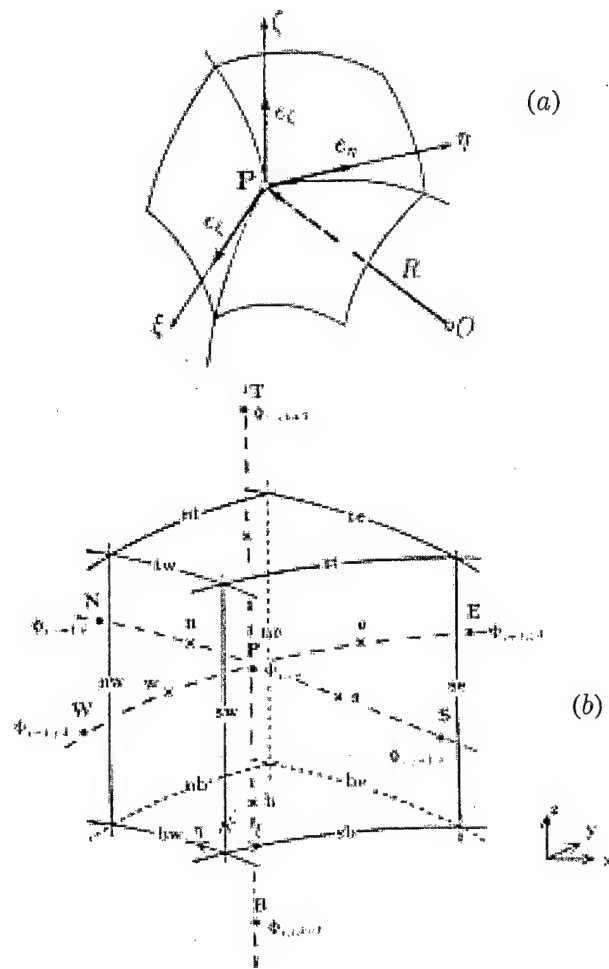
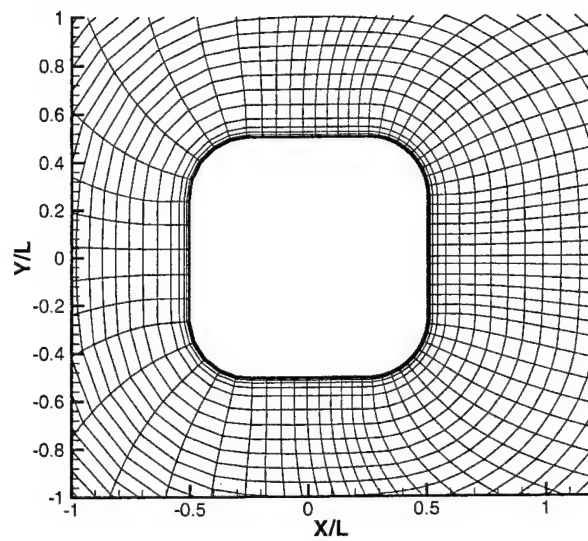
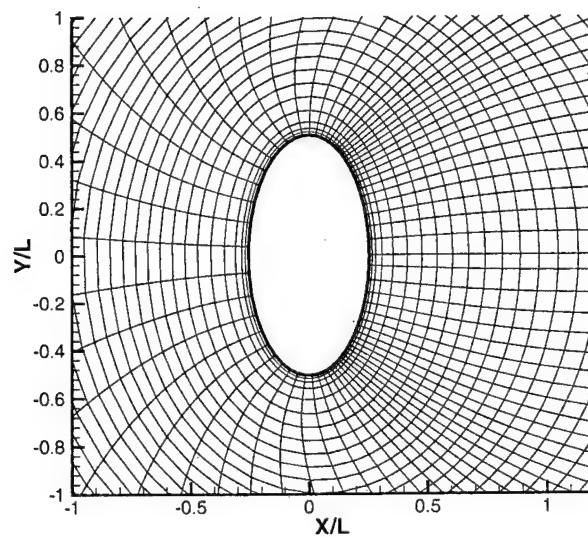


Figure 1: (a) Schematic representing coordinate transformation from the Cartesian system to a curvilinear non-orthogonal system; (b) local volume surrounding the point P , areas bounding the control volume surrounding P given by S^q .



(a)



(b)

Figure 2: Side view of the rounded-corner square (in *a*) and 2:1 ellipse (in *b*). Corner radius of the rounded-corner square is $1/4$ of the body width/diameter D . Flows are from left to right at angle of attack (every fourth grid point shown in the above frames).

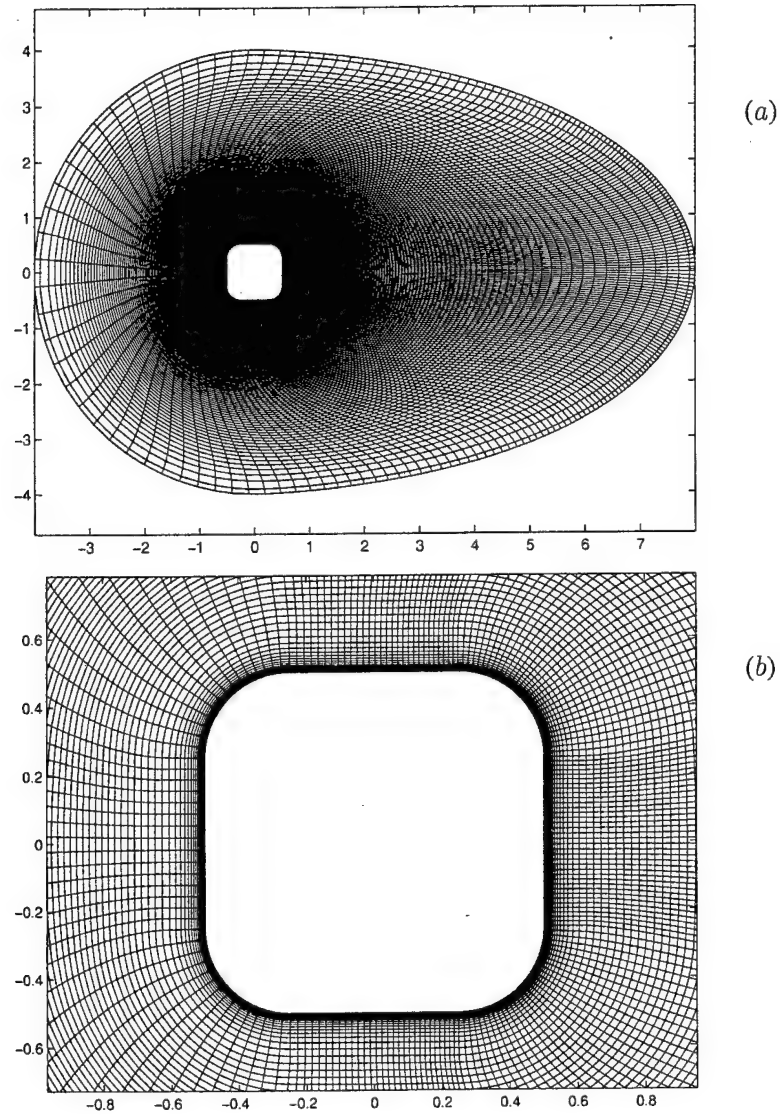


Figure 3: Side view of the structured grid for solution of the flow over the rounded-corner square. Corner radius is $1/4$ of the body width/diameter D . Flow is from left to right at angle of attack. (a) entire computational domain for two-dimensional simulations; (b) zoomed view in the vicinity of the box showing clustering of grid points in the wake region.

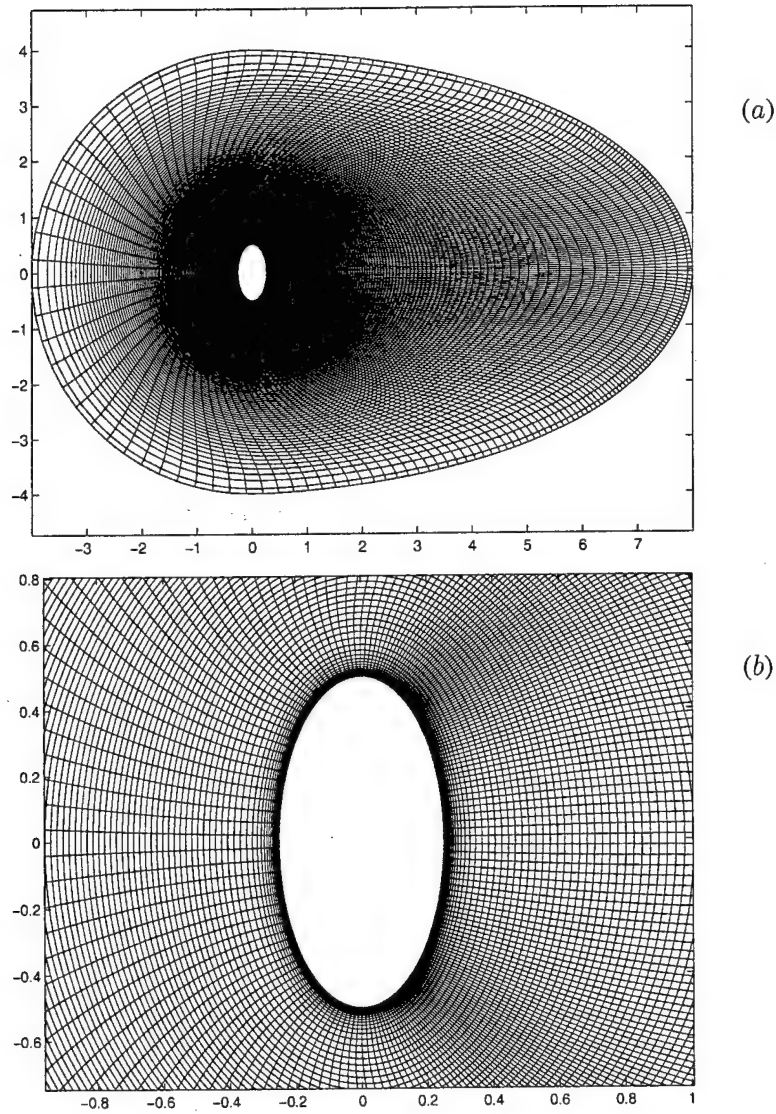


Figure 4: Side view of the structured grid for solution of the flow over the 2:1 ellipse. Flow is from left to right at angle of attack. (a) initial domain for two-dimensional simulations; (b) zoomed view in the vicinity of the ellipse showing clustering of grid points in the wake region.

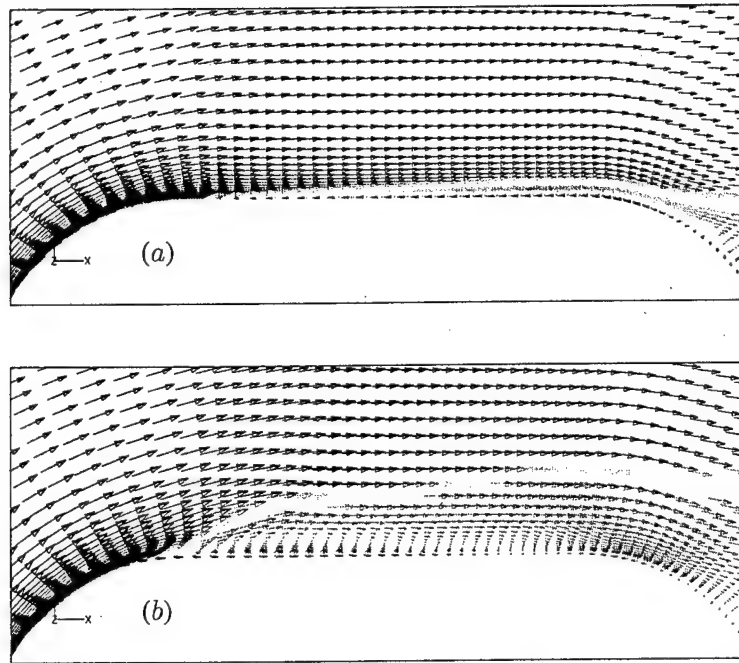


Figure 5: Instantaneous velocity vectors colored by the eddy viscosity ratio, $Re = 5 \times 10^4$, 10° angle-of-attack. (a) turbulent separation – inlet eddy viscosity ratio $\nu_t/\nu = 3$; (b) laminar separation – inlet eddy viscosity ratio $\nu_t/\nu = 0$. Flow detachment near upper rear corner in (a), flow detachment near upper front corner in (b).

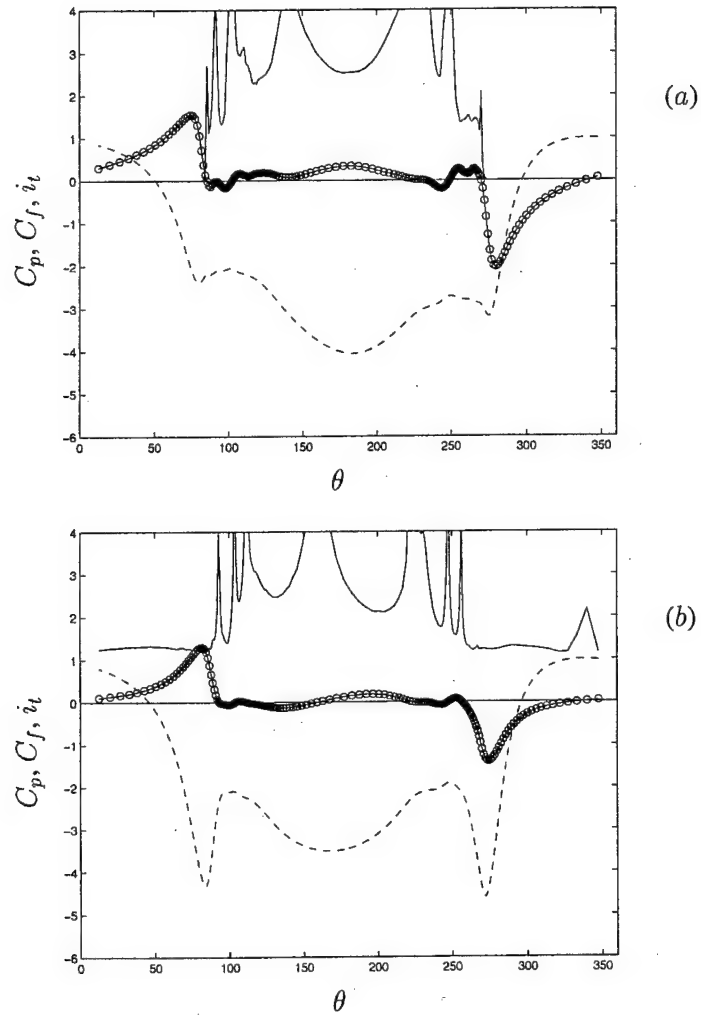


Figure 6: Pressure coefficient, C_p , skin friction coefficient, C_f , and turbulence index i_t around the perimeter of the 2:1 ellipse. $Re = 5 \times 10^4$ in (a), $Re = 8 \times 10^5$ in (b). ---- C_p ; \circ — \circ $1000 \times C_f$; — i_t . Angles are measured from the fore-symmetry stagnation point.

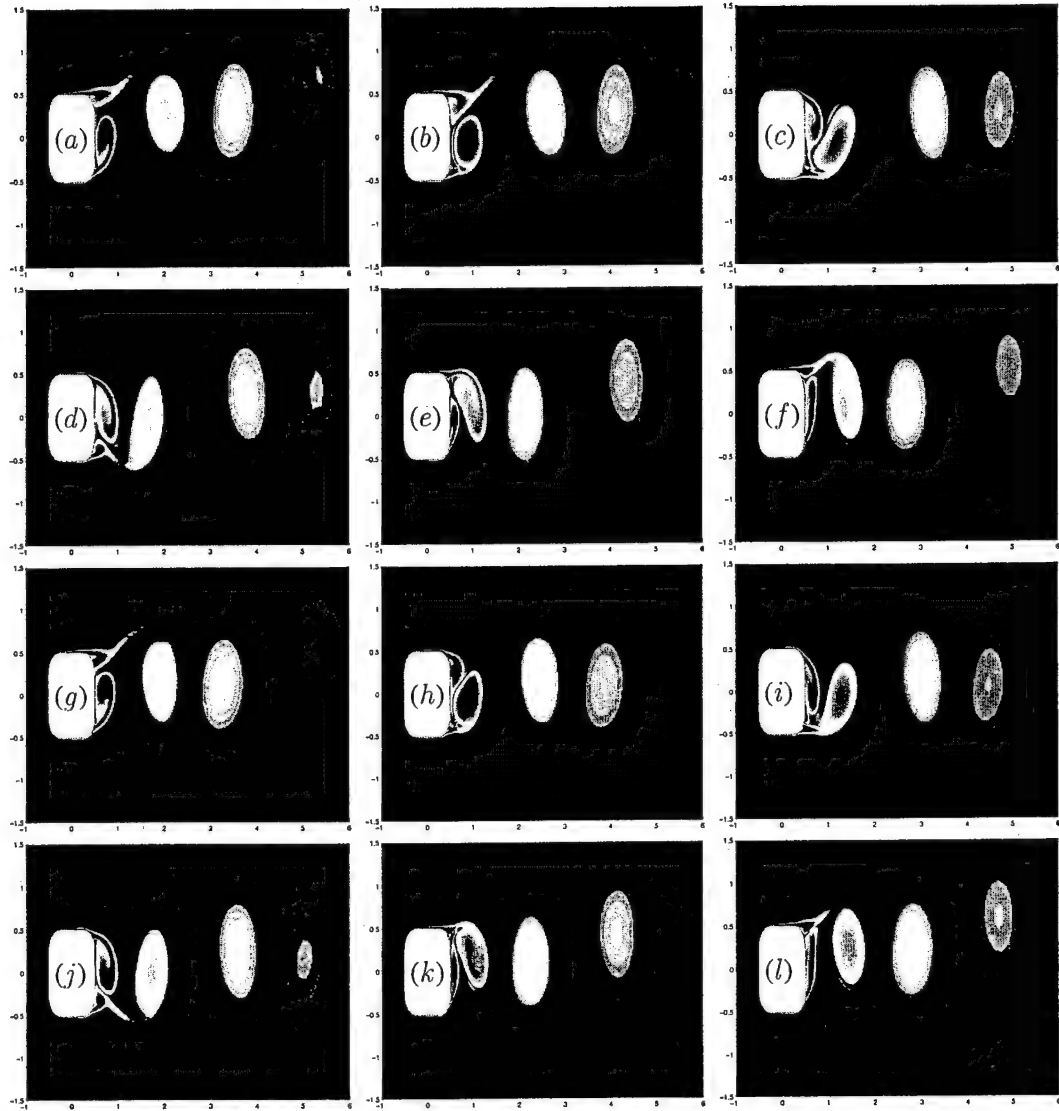


Figure 7: Instantaneous vorticity contours in the wake of the rounded-corner square, $Re = 8 \times 10^5$, turbulent separation. Evolution in time through one shedding cycle evolves from (a) to (l)

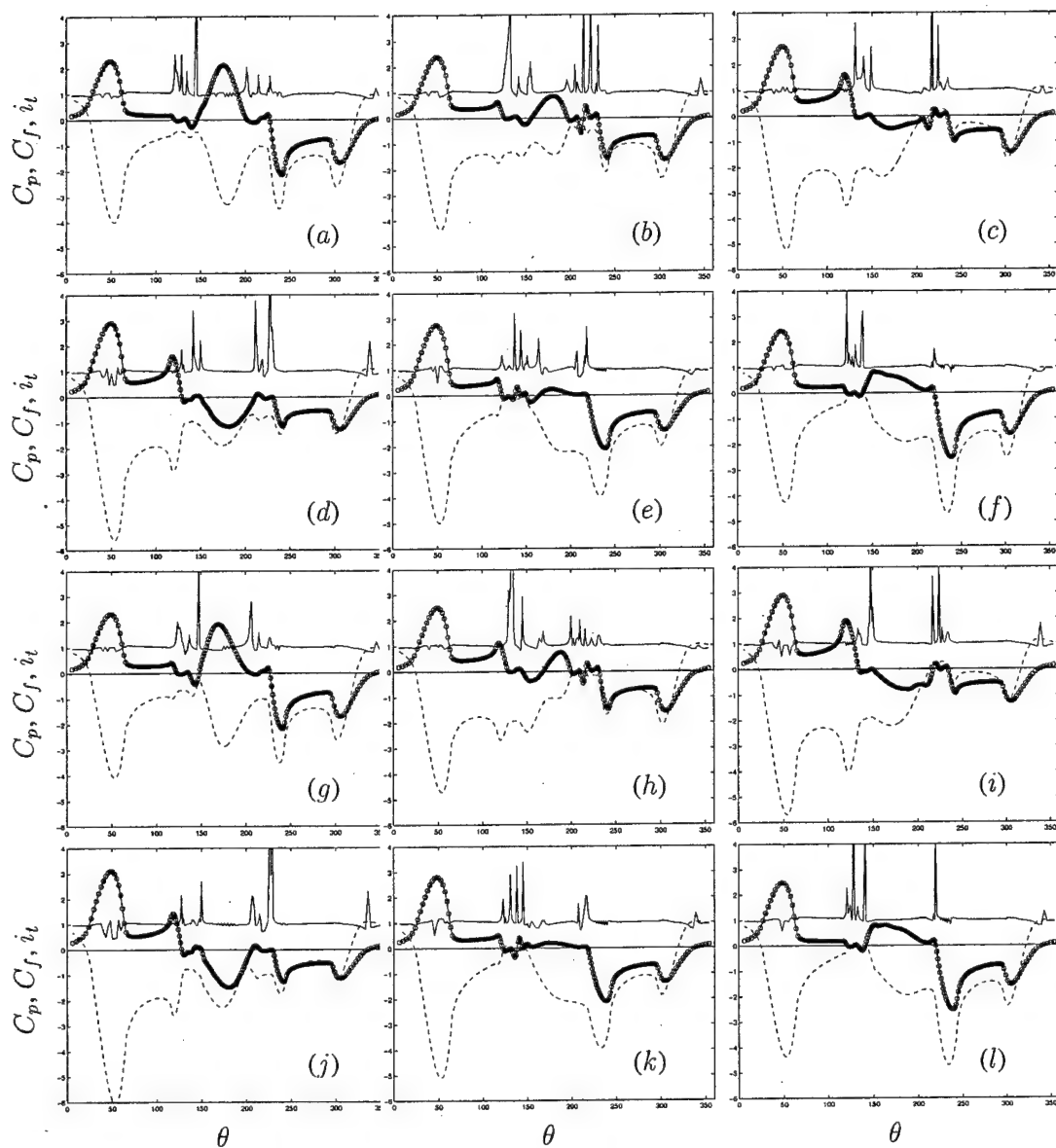


Figure 8: Pressure coefficient, C_p , skin friction coefficient, C_f , and turbulence index i_t around the perimeter of the rounded-corner square, $Re = 8 \times 10^5$, turbulent separation. ---- C_p ; \odot $1000 \times C_f$; — i_t . Angles are measured from the fore-symmetry stagnation point. Evolution in time through one shedding cycle is from (a) to (l).

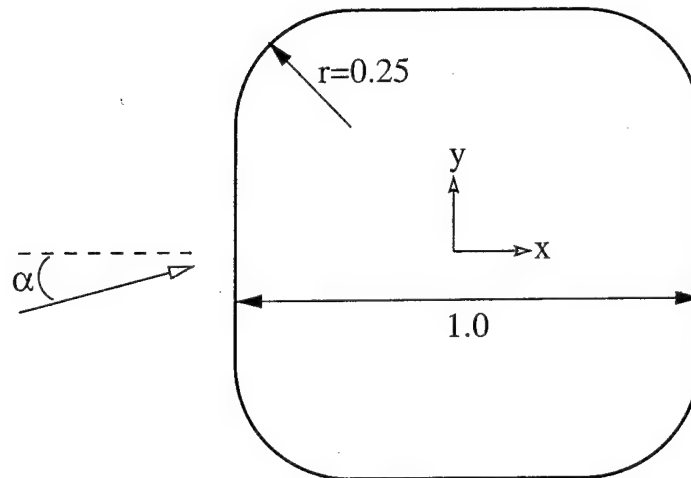


Figure 9: Forebody cross section. Corner radius is 1/4 of the body width/diameter D . Angle of attack measured with respect to the streamwise x axis.

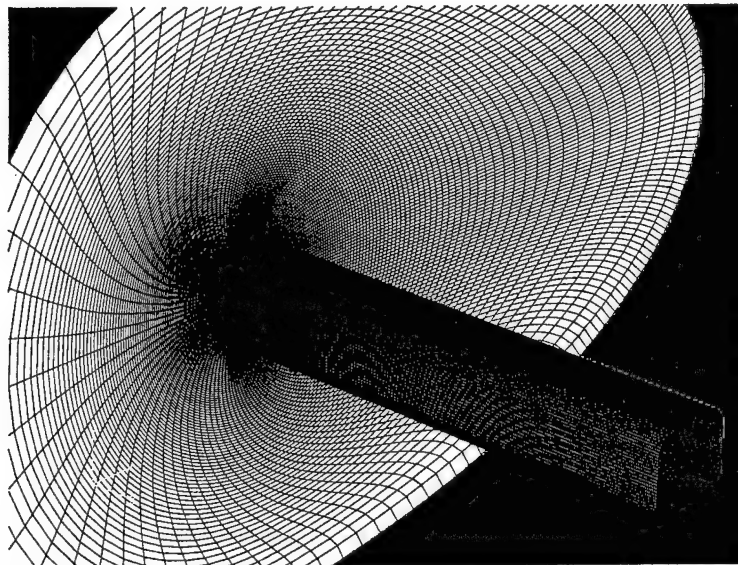


Figure 10: Three-dimensional perspective of the structured grid around the rounded-corner square. Spanwise dimension is six times the forebody diameter as shown above.

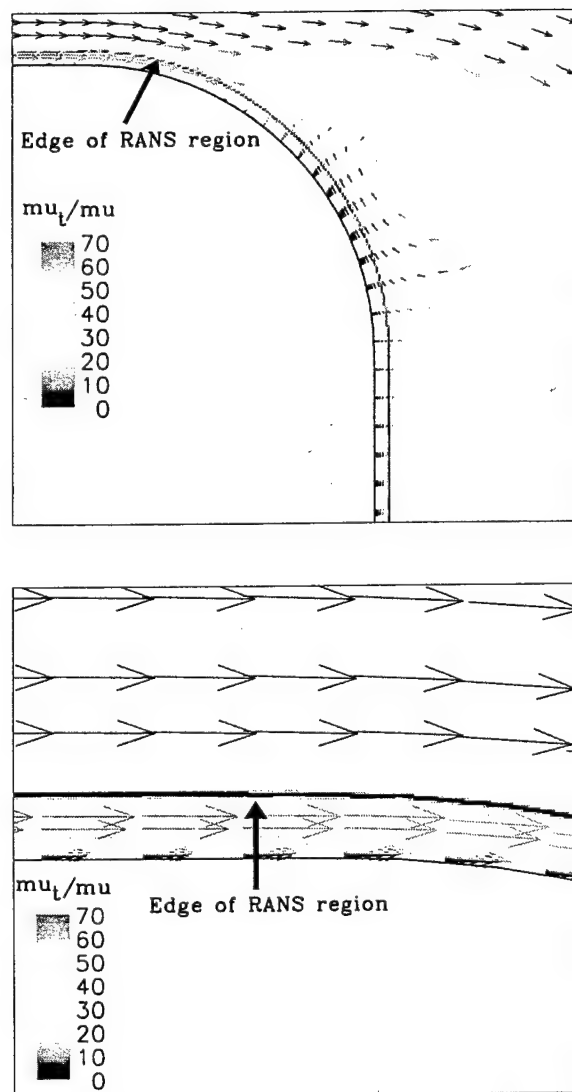


Figure 11: Demarcation between RANS and LES regions, Case 1. Instantaneous velocity vectors colored by the eddy viscosity ratio also shown.

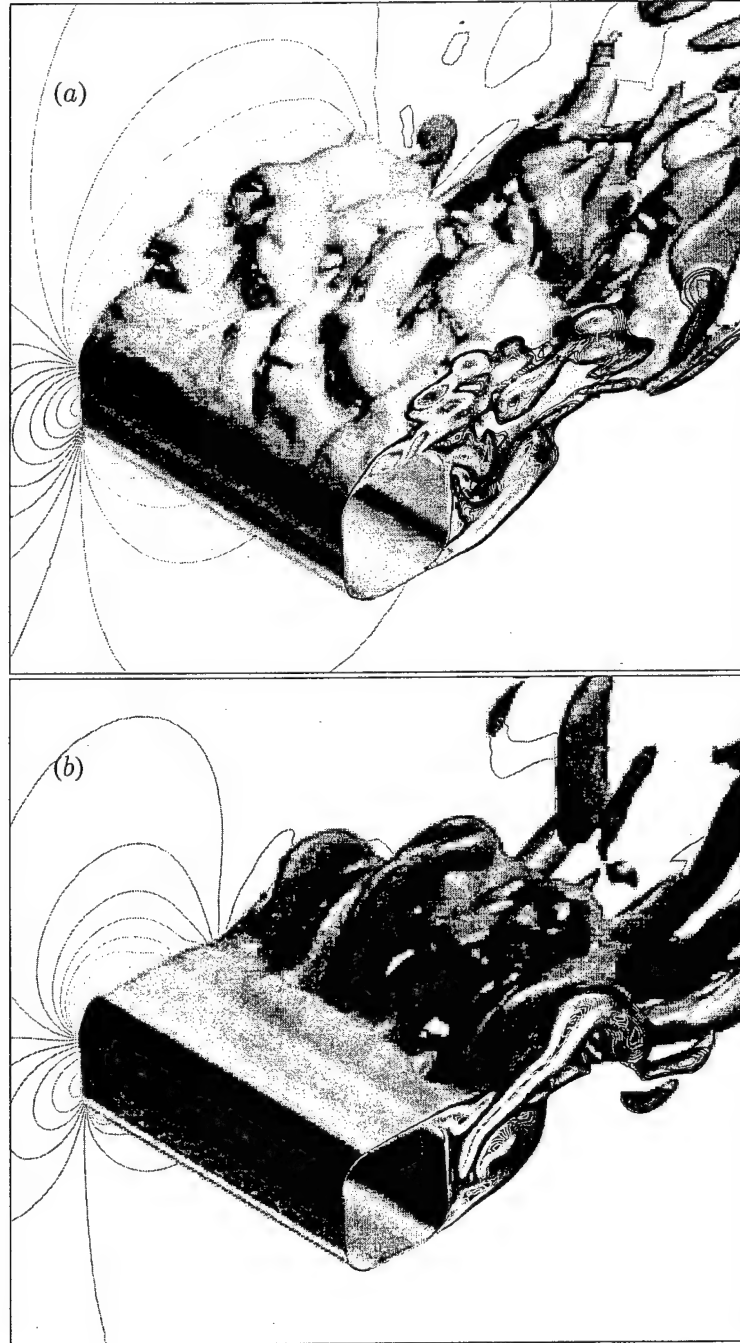


Figure 12: Isosurface of the instantaneous vorticity colored by pressure. Pressure contours projected onto the back plane of each frame. (a) $Re = 1 \times 10^5$ (laminar separation); (b) $Re = 8 \times 10^5$ (turbulent separation).

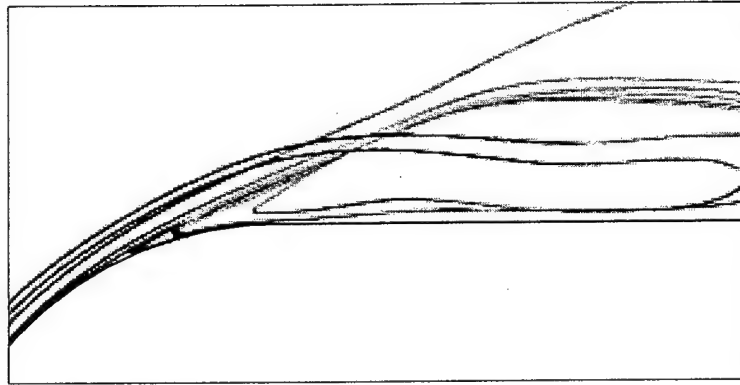


Figure 13: Instantaneous pathlines over the top surface of the forebody colored by the ratio of the turbulent eddy viscosity to the molecular viscosity ν_t/ν . The pathlines are shown from a tripless solution in which the upstream eddy viscosity ratio is zero (blue pathlines in the frame), non-zero values occur in the separated region.

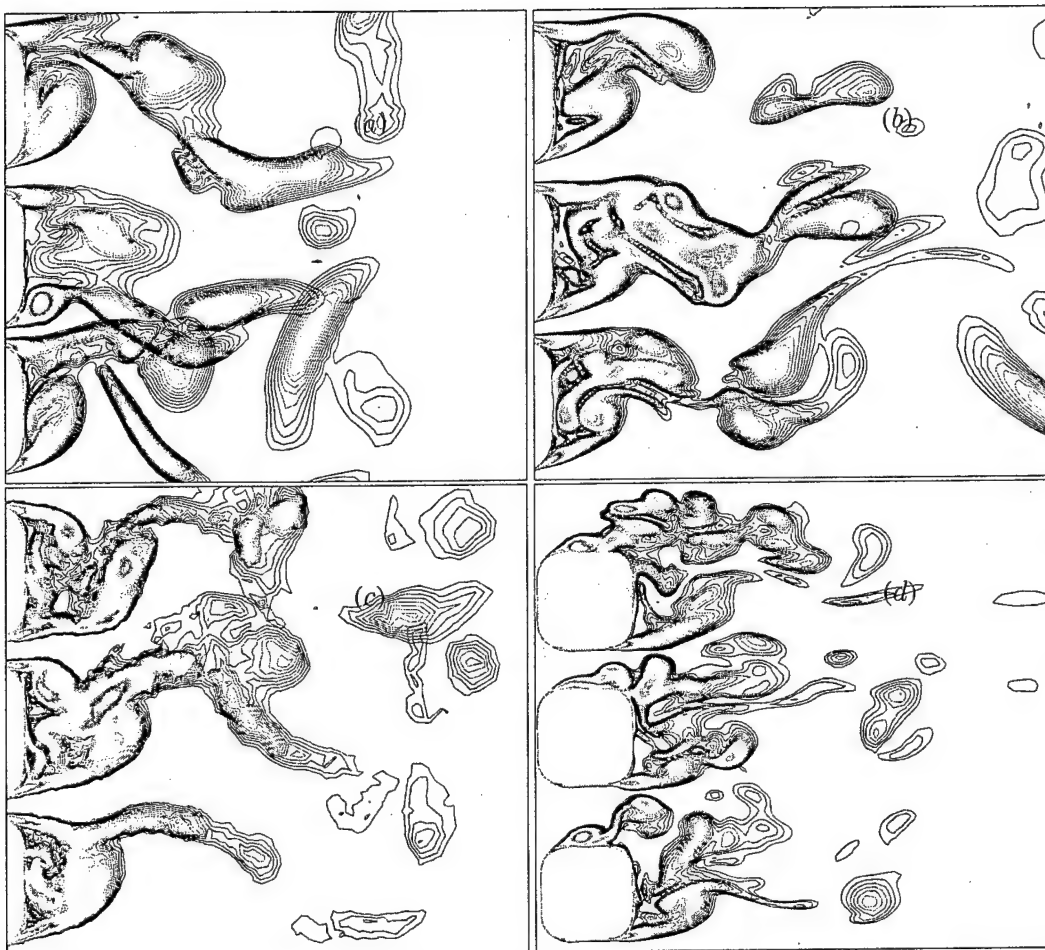


Figure 14: Instantaneous vorticity contours in three spanwise planes along the forebody. Fully-turbulent solutions at $Re = 8 \times 10^5$, 10° angle of attack. (a) Case 1, (b) Case 3, (c) Case 5, (d) tripless solution, simulation parameters correspond to Case 3.

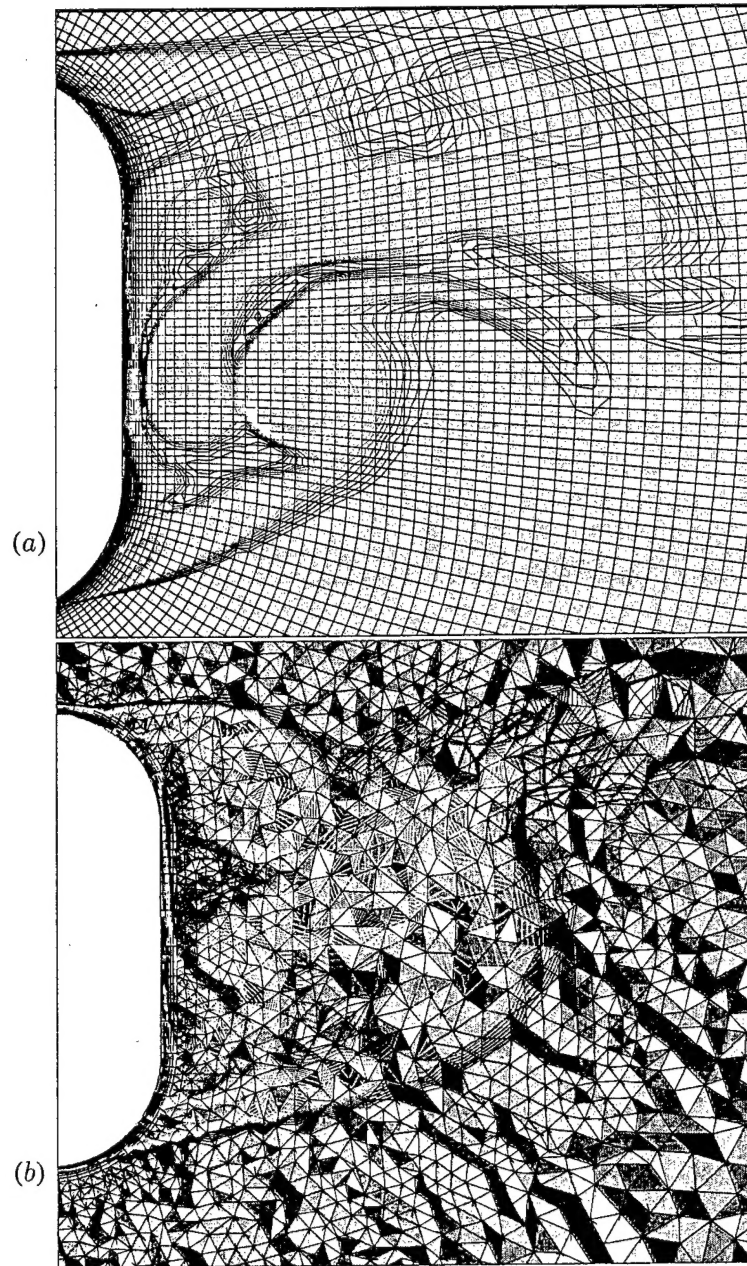


Figure 15: Contours of the instantaneous vorticity in the forebody wake at $Re = 8 \times 10^5$. (a) structured grid, Case 3; (b) unstructured grid, Case 5.

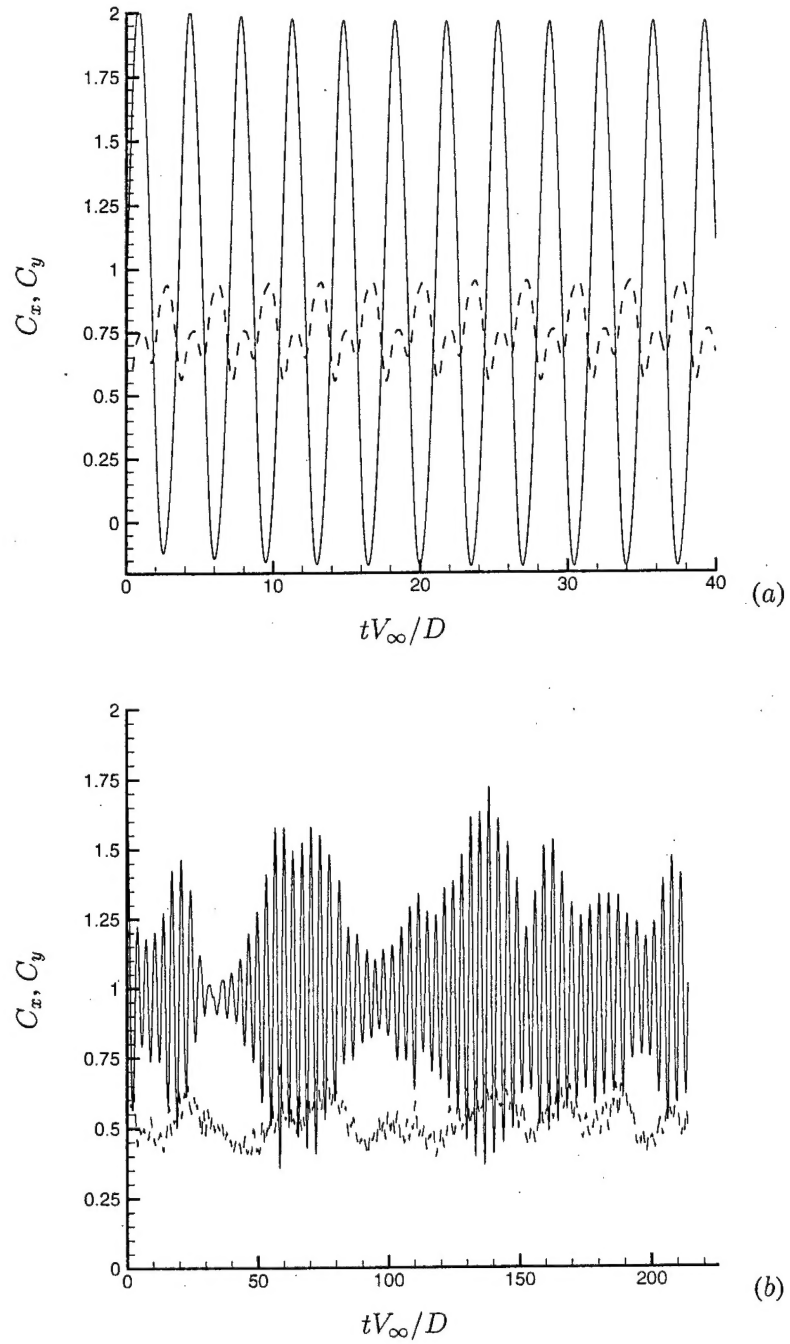


Figure 16: Temporal evolution of the streamwise (C_x) and vertical (C_y) force coefficients. (a) two-dimensional URANS prediction. ---- C_x ; — C_y . (b) DES, Case 2.

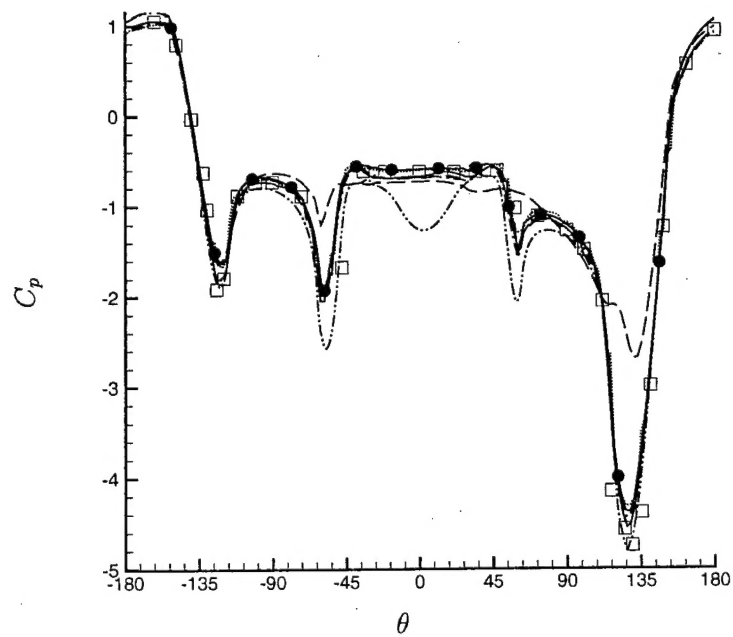


Figure 17: Pressure coefficient distribution around the forebody. Turbulent separation cases, $Re = 8 \times 10^5$. Symbols are measurements from Polhamus *et al.* (1959). — Case 1; ---- Case 3; ——— Case 4; Case 5; - - - - - Case 6; — · — Case 7; ● — ● Case 8.

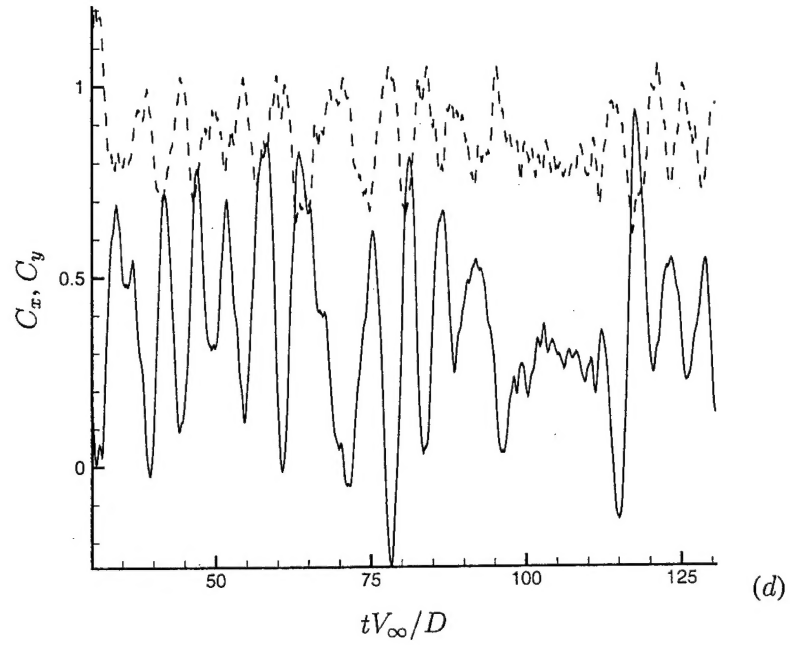


Figure 18: Temporal evolution of the streamwise (C_x) and vertical (C_y) force coefficients. Tripless prediction, simulation parameters correspond to Case 4.

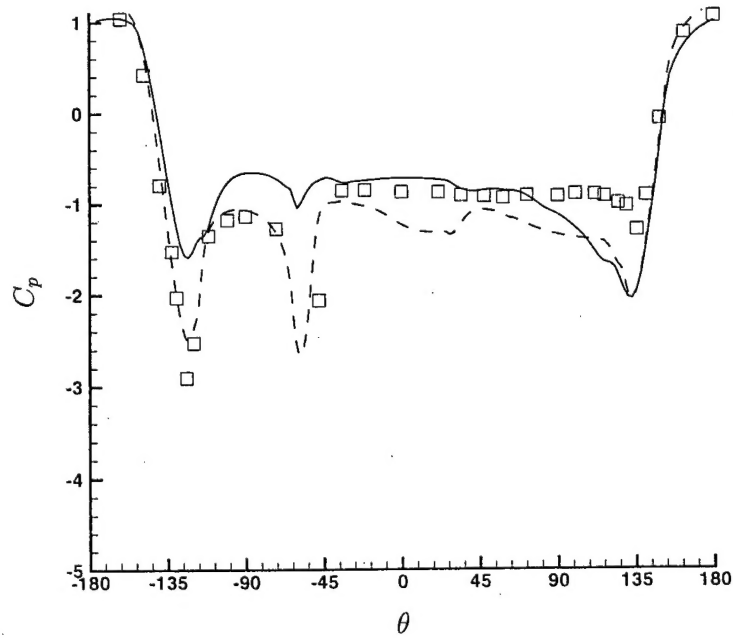


Figure 19: Pressure coefficient distribution around the forebody. Laminar separation cases. Symbols are measurements from Polhamus *et al.* (1959). — Case 4 ($Re = 1 \times 10^5$); ---- Case 7 ($Re = 4 \times 10^5$).